Journal of
Materials Chemistry A

ROYAL SOCIETY
OF CHEMISTRY

REVIEW

View Article Online
View Journal | View Issue

Cite this: *J. Mater. Chem. A*, 2023, **11**, 12499

Solar driven CO_2 reduction: from materials to devices

Lili Wan, Rong Chen, Daniel Wun Fung Cheung, Linxiao Wu and Jingshan Luo *

Received 15th January 2023
Accepted 27th February 2023

DOI: 10.1039/d3ta00267e

rsc.li/materials-a

Solar driven CO_2 reduction for the production of fuels and chemicals is a promising technology for achieving carbon neutrality. Photocatalytic CO_2 reduction, photoelectrochemical CO_2 reduction and photovoltaic-electrochemical CO_2 reduction, are three main approaches for solar driven CO_2 reduction that have attracted a lot of interest in both the academic and industrial communities. However, in spite of the decades of work that have been devoted to this research area, low solar to fuel efficiency, poor product selectivity and unsatisfactory stability continue to impede the application of these three technologies. Herein, we summarize the recent advances in photo-absorbers, catalysts and device designs for solar driven CO_2 reduction and have identified the following requirements that are essential for realizing a highly efficient solar driven CO_2 reduction system: optimized photo-absorbers, tailored catalysts, well-designed devices and the synergistic operation of these three parts. In addition, we provide perspectives for the future development of the solar driven CO_2 reduction field.

10th Anniversary Statement

Congratulations on the 10th anniversary of *Journal of Materials Chemistry A*! The journal was launched in the middle of my PhD study, and its theme fitted well with my research topic. It has accompanied me through my scientific career from a PhD student, postdoc, to my current position as a full professor. I have witnessed the fast growth and expanding impact of the journal, and I am a frequent reader, author, and active reviewer of the journal. Since 2020, I have been an advisory board member of the journal. It is my great pleasure to contribute a review article as the corresponding author to this special issue. As the world's demand for energy and sustainability is continuously increasing, the journal will continue to excel and contribute to the common benefits of human kind.

1. Introduction

1.1 Motivation for CO_2 recycling

The atmospheric concentration of CO_2 has increased by around 100 ppm over the past century due to human activity,[1] mainly the excessive combustion of fossil fuels, which has disrupted the natural carbon cycle and caused severe environmental and ecological problems.[2] Without efficient carbon emission reduction strategies, the concentration of CO_2 in the atmosphere would rise up to 570 ppm by the year 2100, which would lead to an increase of approximately 1.9 °C in the mean global temperature.[3] One of the ideal strategies of CO_2 reduction is converting CO_2 into value-added chemicals and carbonaceous fuels using renewable energy, such as solar energy. It has been estimated that 10% of the solar energy received by the Earth *via* sunlight irradiating 0.3% of the Earth's surface would be sufficient to fulfill the global energy needs for a year.[4] In 1978, Halmann discovered the photo-induced reduction of CO_2 into carbonaceous products on semiconductors,[5] which led to large amount of research focusing on solar driven CO_2 conversion.

1.2 Solar driven CO_2 reduction

Solar driven CO_2 reduction utilizes the energy from sunlight to reduce CO_2 into value-added carbonaceous chemicals, such as CO, CH_4, $HCOO^-$, alkenes and alcohols. Solar driven CO_2 reduction is typically divided into photocatalytic CO_2 reduction (PC CO_2R), photoelectrochemical CO_2 reduction (PEC CO_2R) and photovoltaic-electrochemical CO_2 reduction (PV-EC CO_2R) approaches.

In the PC CO_2R system, CO_2 reduction and oxidation reactions (most commonly the water oxidation reaction) both occur on the surface of semiconductors under light irradiation. Three crucial steps are involved in this process (Fig. 1A).[6–9] In the first step, the semiconductor absorbs incident light with energy equal to or higher than its bandgap and photo-induced electron–hole pairs are subsequently generated. The photo-induced electrons are excited to the conduction band (CB) and the holes remain in the valence band (VB). In the second step, the photo-induced electrons and holes migrate to the surface of the semiconductor, but a large proportion of the electrons and holes may be consumed by bulk recombination and surface

---

Institute of Photoelectronic Thin Film Devices and Technology, Solar Energy Research Center, Key Laboratory of Photoelectronic Thin Film Devices and Technology of Tianjin, Ministry of Education Engineering Research Center of Thin Film Photoelectronic Technology, Renewable Energy Conversion and Storage Center, Nankai University, Tianjin 300350, China. E-mail: jingshan.luo@nankai.edu.cn

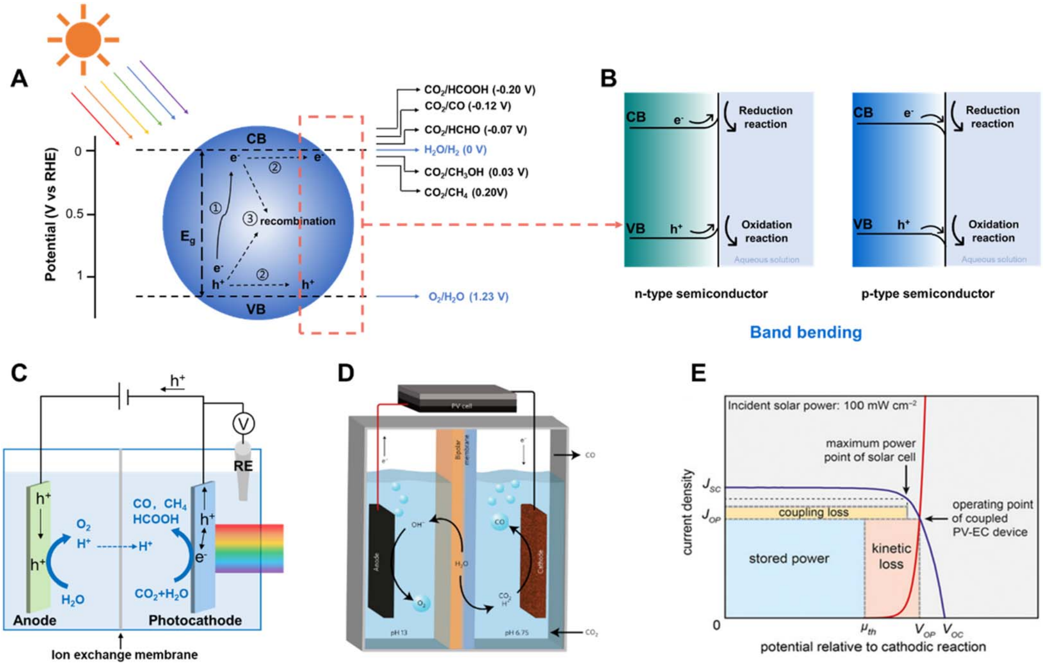

Fig. 1 (A) Schematic of photocatalytic CO_2 reduction, illustrating the three main steps of the process, and (B) band bending of an n-type and a p-type semiconductor at the semiconductor/liquid interface.[12] Copyright 2015, Springer Nature. (C) Schematic of a typical photoelectrochemical CO_2 reduction device. (D) Schematic of the PV-EC CO_2 reduction device.[13] Copyright 2017, Springer Nature. (E) General current density–voltage diagram for a coupled PV-EC system.[14] Copyright 2013, Proceedings of the National Academy of Sciences.

recombination. Photo-induced electrons which successfully migrate to the surface reduce CO_2 into fuels and H_2O into H_2 as the by-product, whilst holes on the surface of the semiconductors oxidize H_2O into O_2. The hydrogen evolution reaction (HER) accompanies the CO_2 reduction due to the similar equilibrium potentials of these half-reactions (Fig. 1A).[10] At the semiconductor–liquid interface, the difference between the Fermi level (E_F) of the semiconductor and the redox potential level of the liquid (electrolyte) (E_R) induces band bending at the semiconductor/liquid interface, which facilitates the separation of photo-generated electron–hole pairs during light irradiation.[11] E_F is close to VB in p-type semiconductors, and it is

Lili Wan received her bachelors degree in Environmental Science from Inner Mongolia University in 2011 and obtained her masters and doctorate degrees in Environmental Science from Nankai University in 2015 and 2019, respectively. During her PhD study, she visited Geoffrey A. Ozin's group at the University of Toronto as an exchange doctoral student for one and a half years, where she focused on photocatalytic CO_2. She is currently a Postdoc at the Institute of Photoelectronic Thin Film Devices and Technology of Nankai University. Her research interests primarily focus on electrochemical and photochemical CO_2 reduction.

Jingshan Luo is a full professor and vice director of the Institute of Photoelectronic Thin-Film Devices and Technology at Nankai University. He received his BSc degree from Jilin University in 2010 and his PhD degree from Nanyang Technological University in 2014. After that, he went to École Polytechnique Fédérale de Lausanne (EPFL) for postdoctoral research with Professor Michael Grätzel. In 2018, he joined Nankai University. He has authored/coauthored more than 120 peer-reviewed publications, which have been cited more than 23 000 times with an H-index of 67. He has received many awards and honors, such as the MIT Technology Review TR35 in China, the 2018–2022 Highly Cited Researcher by Clarivate Analytics, and the Excellent Young Scholar Fund from the National Science Foundation of China. His main research interests are solar water splitting, CO_2 reduction and perovskite solar cells.

typically lower than E_R, which results in a tendency for electrons flowing from the liquid to the semiconductor, building up an electric field in the semiconductor near the interface. This electric field causes band bending at the semiconductor–liquid interface. Therefore, the CB and VB of a p-type semiconductor bend downward, from the semiconductor to the liquid (Fig. 1B), enhancing electron–hole pair separation and facilitating electron transport to the semiconductor–liquid interface, which is critical for improving the photo to electron conversion efficiency.

The PEC CO_2 reduction is generally performed in a cell with two compartments (H-type cell), which mostly consists of a photoelectrode, a counter/dark counter electrode, reference electrode and a membrane (proton- or anion-exchange membrane, for separating the electrolyte of two half-reactions, transferring the protons or the donor of protons). As illustrated in Fig. 1C, photo-induced electrons are generated on the photocathode under light irradiation conditions, transferred to the electrode/electrolyte interface and reduce CO_2 or H_2O into carbonaceous products or H_2, whilst photo-induced holes are transferred from the external circuit to the anode and oxidize H_2O into O_2. Similar to the situation of a semiconductor in contact with an aqueous solution, semiconductors on an electrode exhibit band bending due to equilibration of the semiconductor Fermi level with the redox potential of the electrolyte, which creates a space charge region providing an electric field at the interface of the electrode/electrolyte.[15] The "downward" band bending in the space charge region of the semiconductor enables efficient separation of photo-induced electron–hole pairs, directing electrons toward the electrolyte solution to drive the reduction reaction. The PEC system is different from the PC system because it separates the photo-induced electrons and holes from the surface of one particle to two different electrodes which can be placed in two chambers, allowing further separation of the redox products. The directional flow of the photo-induced electrons and holes reduces the amount of recombination of electrons and holes in the PEC system. In addition, the separation of photo-induced electrons and holes can be further enhanced by applying an external bias. However, the ultimate goal of the PEC CO_2 reduction system is to construct a bias-free two-electrode cell, which is driven by the solar irradiation.[16] It is challenging to construct photoelectrodes offering sufficient photo-voltage and with suitable conduction and valence band edges.

Photovoltaic (PV) driven electrochemical (EC) CO_2 reduction, as another key strategy for converting solar energy into fuels and chemicals, employs photo-electrons provided by PV to reduce CO_2 at the cathode in the EC cell (Fig. 1D).[17] It combines the benefit of photovoltaics that it is a proven technique for photoelectric conversion with high efficiency and the advantage of electrocatalysis that it is a relatively mature technology close to practical application. The coupling of two distinct systems, both of which can be optimized independently, makes it an attractive integrated system.[18] Collaborative coupling of the PV cell and EC is essential to achieve a highly efficient integrated system. It is better to operate the PV-EC system close to the maximum power point of the PV device, which is located at the intersection point of the electrocatalytic *J*–*V* curve of the electrocatalyst and PV cell close to the maximum power point of the PV device (Fig. 1E). Otherwise, the impedance mismatch significantly curtails the power available to run the EC cell.[8,14]

1.3 Strategies for improving the efficiency of solar driven CO_2 reduction systems

Although PC, PEC and PV-EC systems are all driven by solar energy, they are intrinsically different from each other. The major difference between the PC system and the PEC system is the directional flow of the photo-induced electrons and holes in the PEC system and that the direction of the built-in electric field can be interchanged through the adjustment of the applied bias voltage. The Fermi level of semiconductors will move up or down when an external potential is applied and the band bending will therefore invert to form an accumulation region instead of a depletion region. This increases the band bending and enhances the electron–hole pair separation and interfacial charge transfer.[8] Different from PC and PEC systems, the PV-EC system decouples the processes of solar energy conversion into electricity and redox reactions driven by electricity, which makes it easier to optimize the system efficiency by improving the efficiency of the two parts, PV and EC cell, separately.

However, apart from their differences, the three solar driven CO_2 reduction systems also share some common key elements. They all require photo-absorbers to convert solar energy, catalysts to accelerate the reaction kinetics and a well-designed device for realizing a highly efficient system. The first requirement for a highly efficient solar driven system (except for the PV-EC system) is a befitting photo-absorber with suitable band gap and band positions, which decide the absorbed light spectrum and the redox potential of the photo-induced electrons and holes, respectively. This is not a limitation for the PV-EC system because the photon to electron conversion is decoupled from the electrons involved catalysis. The active components, most commonly cocatalysts, are used to accelerate the reaction kinetics, improve product selectivity, and enhance the surface charge carrier transport.[19] A well designed device with suitable characteristics also promotes the efficient utilization and conversion of solar energy. Therefore, materials and device designs are the two key aspects for realizing an efficient solar driven CO_2 reduction system.

2. Materials for solar driven CO_2 reduction

2.1 Photo-absorbers

The photo-absorbers are fundamental materials for a solar driven CO_2 reduction system, which undertake the most important step of photo-absorption and conversion. Two basic properties are required for the photo-absorbers in PC and PEC systems: (i) the band gap of the semiconductors is better to be located in the range of 1.6 eV to 1.7 eV, (ii) the position of the CB and VB should be thermodynamically more negative and positive to the equilibrium potentials of CO_2 reduction and water oxidation, respectively (Fig. 2A). For the single absorber system, the semiconductors must inherently satisfy the above properties concurrently. The multi-junction photo-absorber, such as the Z-scheme structure, type II structure and p–n junction can be adopted in PC and PEC systems for CO_2 reduction when one of the semiconductors has a suitable CB and the other has an appropriate VB (Fig. 2B–D). Transition metal oxides, Si, III–V and II–VI photo-absorbers, perovskite materials, carbon nitrides, metal–organic frameworks and metal complexes are generally employed as photo-absorbers in PC and PEC systems.[20] Most semiconductors in PC systems can also be adopted as the photo-absorbers in PEC systems. The photovoltaic materials functioning as a photovoltaic cell in the PV-EC system were also introduced into PC and PEC systems as photo-absorbers in recent research studies.[21] Here, we discuss some representative semiconductors to demonstrate the importance of photo-absorbers in a highly efficient solar driven CO_2 reduction system.

2.1.1 Transition metal oxides. Titanium dioxide (TiO_2), as a typically conventional photo-absorber, has attracted wide interest owing to its non-toxicity, low cost and good chemical stability. However, its intrinsic property of having a wide bandgap (~3.0 eV) leads to a narrow absorption range, which results in low efficiency.[24] Thus, it is essential to improve the solar to fuel (STF) efficiency of TiO_2 by reducing its bandgap and increasing the lifetime of charge carriers.[25] Strategies such as facet engineering,[26] particle size and morphology control,[27] elemental doping,[28] surface modification[29] and construction of heterojunctions with other semiconductors[30] are commonly employed for modifying the physicochemical properties of TiO_2. Yu *et al.* reported an *in situ* surface modification of polydopamine (PDA) on TiO_2 and systematically investigated the effect of wrapped PDA on the photocatalytic CO_2 reduction activities.[29] By constructing an S-scheme heterojunction, the system achieved a methane yield of 1.50 μmol h^{-1} g^{-1}. Apart from CO_2 reduction in a PC system, TiO_2, an n-type semiconductor, was first applied in the PEC system for water splitting by Fujishima and Honda in 1972.[31] They further reported a PEC for CO_2 reduction using TiO_2 in water, which could generate small amounts of formate and methanol.[32] Since then, TiO_2 has been utilized as a photoanode, photocathode or as the passivation layer in PEC systems. Jing *et al.* utilized multifunctionalized TiO_2 and Co-Pi/W:$BiVO_4$ films as the photocathode and photoanode respectively, with methanol obtained as the major liquid product.[33] Owing to its high stability in aqueous environments, TiO_2 can also be used as a protection layer to prevent the direct contact of the electrode with the electrolyte. In addition, in terms of photoelectrochemical thermodynamics, TiO_2 has a staggered type-II band offset, which promotes the PEC reduction reaction through the transport of photoexcited electrons *via* TiO_2. Chan *et al.* constructed a TiO_2-coated $CuFeO_2$ and CuO mixed (ClFDH-TiO_2|CFO) photocathode with a surface modified layer of formate dehydrogenase.[34] In this structure, the TiO_2 layer not only enhanced the PEC stability, but also facilitated the transfer of photo-excited electrons from CFO to ClFDH. TiO_2, as a stable semiconductor with a wide bandgap, is a valuable semiconductor that can be utilized as a protection layer and photo-absorber and it is also suitable for constructing heterojunctions. Strategies for increasing the performance of TiO_2-based semiconductors are necessary, such as reducing the transparency in the visible range to obtain a more suitable protection layer,

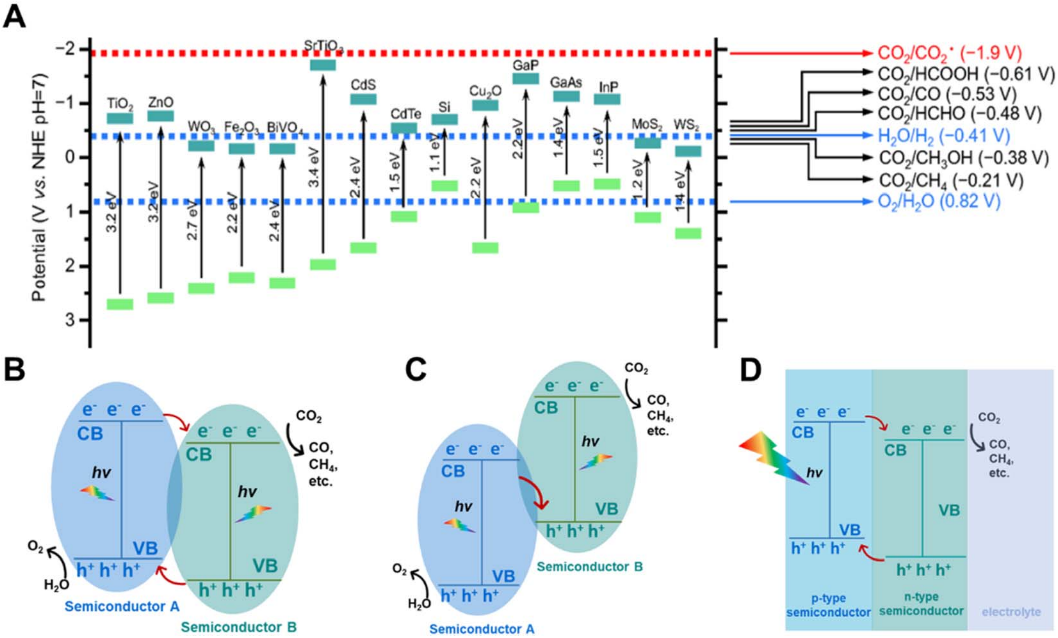

Fig. 2 (A) Conduction band and valence band potentials of several typical semiconductors relative to the standard redox potentials of CO_2 reduction in water at pH 7.[22] Copyright 2018, Science China Press and Springer-Verlag GmbH Germany. (B) Type II heterostructure semiconductors, (C) Z-scheme heterostructure semiconductors, (D) semiconductors constructed as a p–n junction.[23] Copyright 2020, Wiley.

improving the stability in a chemical environment by a new synthetic method of amorphous state and obtaining a longer electron lifetime by efficient charge separation.

Cuprous oxide (Cu_2O) is a p-type semiconductor with a bandgap of 2.0–2.2 eV and a suitable conduction band for CO_2 reduction (Fig. 2A), which makes it an attractive semiconductor for solar driven CO_2 reduction.[35] In 1989, Tennakone *et al.* found that methanol was produced from CO_2 in a PC system on Cu_2O powders under full spectrum illumination from a mercury lamp.[36] However, Cu_2O is unstable under aqueous conditions and light illumination due to the oxidation or reduction of Cu_2O into CuO or Cu, respectively. The efficient strategies of preventing the photo-corrosion of Cu_2O are constructing heterojunction structures, employing co-catalysts to improve the separation and transfer of photo-excited charge carriers or employing a protection layer to prevent direct contact with the electrolyte. Grela *et al.* synthesized octahedral Cu_2O covered with TiO_2 nanoparticles (Cu_2O/TiO_2) and investigated its photocatalytic CO_2 activity in humidified CO_2.[37] As illustrated in Fig. 3A, the p–n heterojunction consisted of Cu_2O and TiO_2, preventing the photo-corrosion of Cu_2O. A higher stability and CO production rate were achieved when using the Cu_2O/TiO_2 p–n heterojunction compared to the individual component materials (Fig. 3B). A ternary Ag–Cu_2O/ZnO nanorod (NR) hybrid structure was also reported by Xu and co-workers. The Z-scheme formed between Cu_2O and ZnO facilitated the photogenerated charge separation and the Ag nanoparticles on Cu_2O promoted the electron transfer, leading to a higher photocatalytic CO_2 reduction activity.[38] Similar strategies were also widely employed in PEC systems. A buried p–n heterojunction structured photocathode (Fig. 3C) composed of Cu_2O/AZO/TiO_2 with a rhenium bipyridyl co-catalyst was investigated by Grätzel and co-workers.[39] The Cu_2O and AZO were combined to create a p–n junction which promoted the separation of photo-excited charge carriers and the TiO_2 further prevented the contact of Cu_2O with the electrolyte. The Cu_2O photocathode exhibited an almost 100% faradaic efficiency (FE) of CO and 5.5 hour stability in anhydrous MeCN with 2 mM Re(tBu-bipy)$(CO)_3$Cl and 7.5 M MeOH for CO_2 reduction (Fig. 3D).

In a recent study, Toma *et al.* investigated the degradation mechanisms of the Cu_2O photoelectrode when used for CO_2 reduction.[40] The transformation of Cu_2O into Cu^{2+}–OH in aqueous solution under illumination, which was contributed by both the photo-excited electrons and holes, prevented the transfer of photo-excited electrons from Cu_2O to the catalysts (Fig. 4A and B). Therefore, the authors replaced the aqueous electrolyte with 2 mM Re(tBu-bipy)$(CO)_3$Cl and 7.5 M MeOH, and a heterostructure system consisting of a WO_3/Fe_2O_3 bilayer as the hole transfer layer and Cu_2O as the photo-absorber was constructed (Fig. 4C) to facilitate the transfer of photo-excited holes. A FE of C_2H_4 of 60% over 3 h was achieved using this system (Fig. 4D).

Cu_2O, as an attractive semiconductor with a near ideal band structure for the CO_2 reduction reaction, still has a lot of potential for wider application,[35] and future efforts can be focused on improving its stability by introducing newly developed protection layers, and improving its efficiency by constructing optimized p–n junctions and nanostructures.

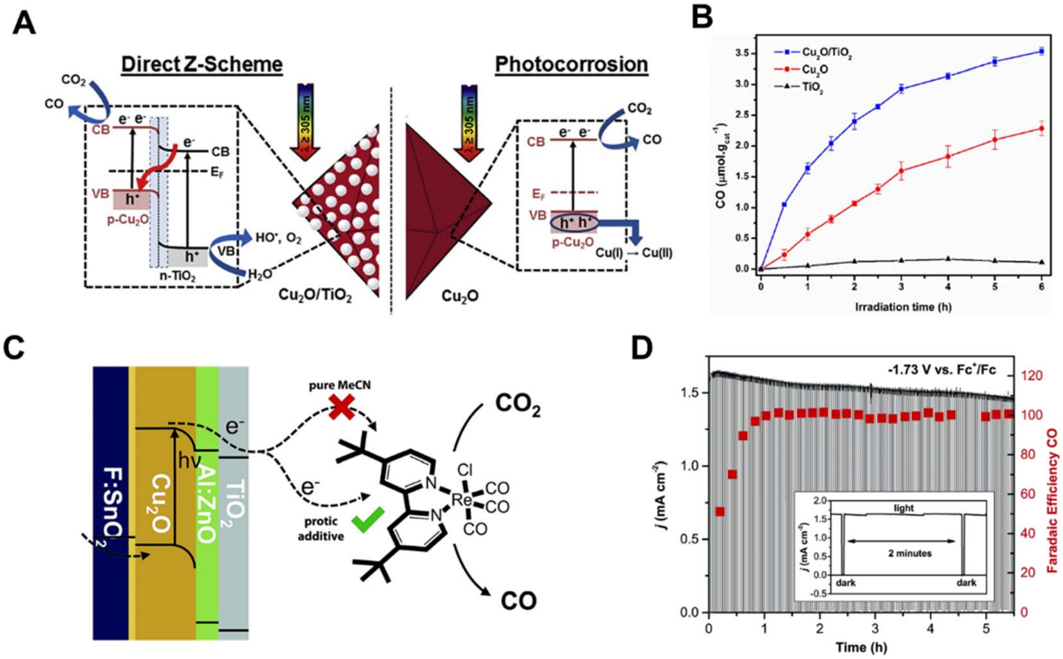

Fig. 3 (A) Schematic illustration of a direct Z-scheme consisting of Cu_2O and TiO_2, (B) photocatalytic CO_2 reduction performance of TiO_2, Cu_2O and Cu_2O/TiO_2.[37] Copyright 2017, Elsevier. (C) Schematic of the photoelectrochemical CO_2 reduction process involving TiO_2 protected Cu_2O photocathodes with a Re-based molecular co-catalyst, (D) cathodic current density and FE of CO on a Cu_2O photocathode under chopped light illumination at a constant potential of −1.73 V *vs.* Fc+/Fc in MeCN with 2 mM Re(tBu-bipy)$(CO)_3$Cl and 7.5 M MeOH.[39] Copyright 2015, Royal Society of Chemistry.

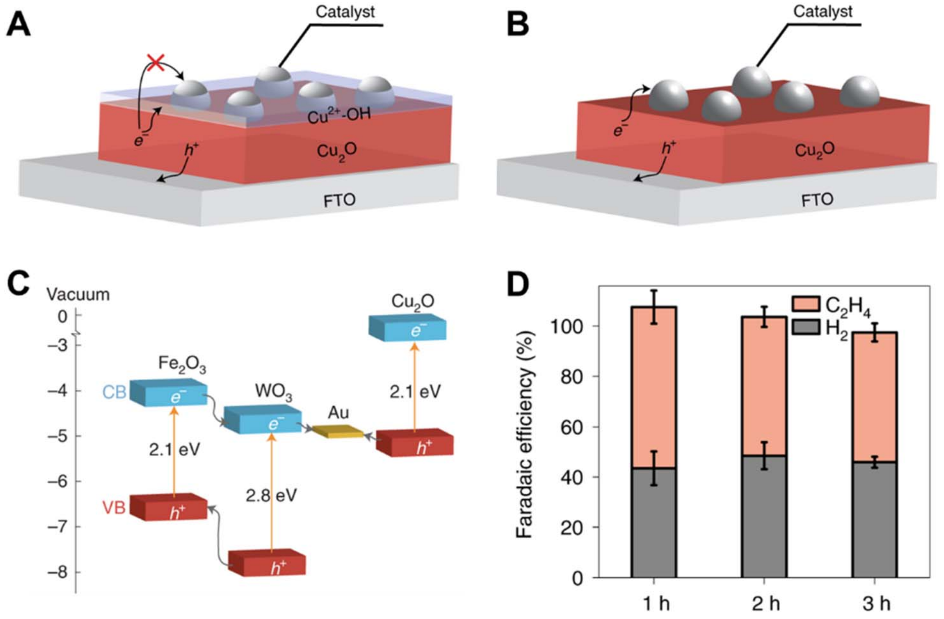

Fig. 4 (A) Schematic of the charge transfer between Cu_2O and the catalysts, in the presence of Cu^{2+}–OH (aq) species. (B) Schematic of the charge transfer between Cu_2O and the catalysts, in the absence of Cu^{2+}–OH (aq) species. (C) The band diagram of suitable candidates for constructing the Z-scheme system. (D) faradaic efficiencies on the Ag/Cu_2O/ZS/FTO photocathode for CO_2R over time at −1.2 V *versus* Fc^+/Fc under AM 1.5G simulated sunlight (100 mW cm^{-2}) using 0.1 M Bu_4NPF_6 as the electrolyte and 0.1 M TEOA as the proton donor in AcCN solution (CO_2 saturated).[40] Copyright 2021, Springer Nature.

Delafossite materials of the general stoichiometry ABO_2 are a new class of promising photocatalysts for solar driven CO_2 reduction. Symmetry breaking in these materials, by chemical substitution, modifies the band structure of the solid. Therefore, the photocatalytic performance of delafossites can be enhanced through engineering by adjusting the alignment of its band edges. Bocarsly *et al.* found that the addition of a Mg^{2+} dopant increases the conductivity of $CuFeO_2$. Mg-doped $CuFeO_2$ was demonstrated to have a conduction band edge at −1.1 V *vs.* SCE (pH = 6.8) and the ability to reduce CO_2 to formate with an underpotential of 400 mV.[41] In 2019, Park and co-workers mixed copper and iron oxide (CuO/$CuFeO_2$; CFO) to form bulk heterojunction films, which were capable of converting CO_2 and water into C1–C6 aliphatic acid anions and O_2 with a solar-to chemical energy conversion (STC) efficiency close to 3% under simulated sunlight in the absence of any sacrificial chemicals or electrical biases.[42]

2.1.2 Silicon. Silicon (Si) has a great potential as a photoabsorber because it is an earth-abundant element with several desirable properties, including a narrow energy band gap of *ca.* 1.2 eV, high carrier mobility, stability over a wide pH range, nontoxicity, and commercial availability. In 1998, p-type silicon (p-Si) electrodes modified with small metal (Cu, Ag, or Au) particles were investigated in CO_2-saturated aqueous electrolytes under illumination, on which methane, ethylene, carbon monoxide and other carbonaceous products were produced.[43] Although planar p-Si is promising, charge carrier recombination occurs due to the short diffusion length of the minority carriers in the same absorber thickness. A wire-array geometry possesses long optical pathlengths for efficient photon absorption and increased collection efficiency for the minority carriers. Park's group fabricated Sn-coupled p-Si nanowire arrays and utilized them for photoelectrochemical CO_2 conversion. Under light irradiation (AM 1.5G, 100 mW cm^{-2}), the amount of formate produced on the p-Si wire arrays was doubled compared to that observed on the planar p-Si.[44] Different from most of the previous studies, which mainly reported a selectivity for C1 products, some recent studies depicted a high selectivity for C2 products on Si-based photocathodes. Zheng *et al.* fabricated a Si/ZnO_v/Cu_xO p–n–p heterojunction for photoelectrochemical CO_2 reduction with a high ethanol selectivity.[45] The Si/ZnO_v/Cu_xO photocathode enabled the transfer of tunneling photoelectrons through the electron-permeable tunnel formed in defect levels of ZnO_v and Cu_xO (Fig. 5A) and it exhibited a FE for ethanol of more than 60% with a current density of around 1 mA cm^{-2} (Fig. 5B). A hybrid photocathode composed of silicon nanowires (SiNWs) embedded with copper nanoparticles also achieved a FE for C_2H_4 of 25% with a current density of 2.5 mA cm^{-2} at −0.50 V *vs.* RHE under AM 1.5G light illumination and maintained a good stability over 50 h (Fig. 5C–G).[46] Apart from its utilization as a photoelectrode, Si is also an excellent material for photovoltaics and Si solar panels are favored in PV-EC systems for CO_2 reduction.[47,48] To achieve a high STF conversion efficiency, the Si photovoltaic cell can be connected in series to drive electrochemical CO_2 reduction. Thus, the further development of Si as a photo-absorber will be broad due to its attractive properties. It will be a promising way to expand the application of Si as a photo-absorber by constructing homojunctions of p–n^+, n^+–p–p^+ and p^+–p–n^+ structures or hybrid structures of homojunctions and heterojunctions, such as p–n^+-

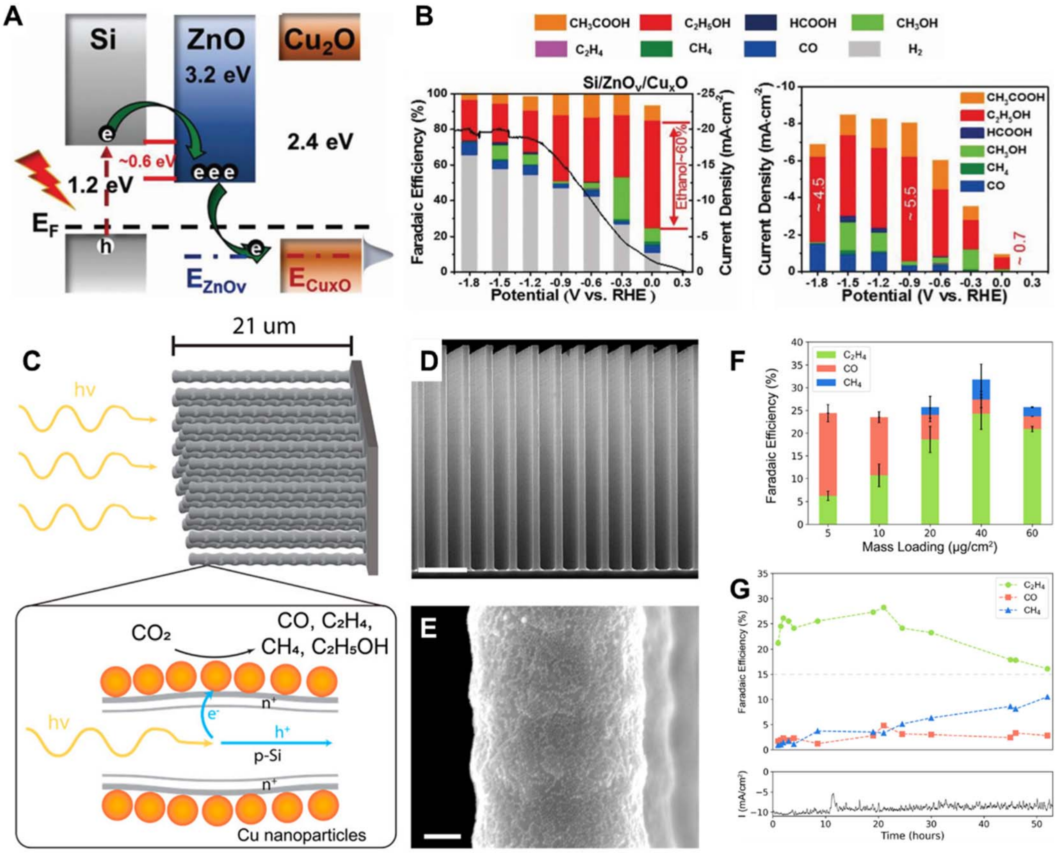

Fig. 5 (A) A schematic illustration of the band structure of Si/ZnO$_V$/Cu$_x$O, (B) FE of photoelectrochemical CO_2 reduction on Si/ZnO$_V$/Cu$_x$O in CO_2-dissolved 0.1 M $KHCO_3$ under airmass 1.5G (left), partial photocurrent densities and products obtained on Si/ZnO$_V$/Cu$_x$O (right).[45] Copyright 2022, Wiley. (C) A schematic of the CuNPs/Si nanowire arrays, illustrating the dopant layer and the charge separation processes occurring within the arrays, (D) SEM image of the Si NW array (scale bar 4 μm), (E) the corresponding SEM image with greater magnification (scale bar 100 nm), (F) FE of CO_2 reduction products as a function of mass loading of Cu NPs at −0.50 V *vs.* RHE. (G) Stability test of the CuNP/SiNW photocathode operating at −0.50 V *vs.* RHE at 1 Sun using a loading mass of Cu NPs of 40 μg cm^{-2}.[46] Copyright 2022, American Chemical Society.

Cu_2O or n$^+$–p–p$^+$-GaN. The optimized homojunction or heterojunction structures of Si materials will not only improve its activity, but also increase the lifetime from several to thousands of hours.

2.1.3 III–V group photo-absorbers. A typical III–V group semiconductor is gallium phosphide (GaP), which has a band gap of 2.3 eV and a highly negative conductive band suitable for most CO_2 reduction reactions.[32] In 1978, the photoelectrochemical CO_2 reduction under aqueous conditions was carried out on GaP under 365 nm illumination with an applied overpotential of −1.4 V (*vs.* SCE) by M. Halmann.[5] Afterwards, Bocarsly *et al.* reported a p-GaP semiconductor with a homogeneous pyridinium ion catalyst for reducing CO_2 into methanol with near 100% FE in 0.1 M acetate buffer containing 10 mM pyridine maintained at pH 5.2 (Fig. 6A and B).[49] However, photo-corrosion still presented a problem for GaP when used under aqueous conditions. Cronin *et al.* constructed a TiO_2-passivated p-GaP photocathode and investigated the effects of the thickness of TiO_2 p-GaP on the photocatalytic CO_2 reduction performance and stability (Fig. 6C and D).[50] Methanol was detected when using the TiO_2-passivated p-GaP photocathode, but the amount tripled when the pyridine catalyst was introduced to the surface, demonstrating that the pyridine catalyst helped to lower the energy barriers of the reaction. Carter *et al.* further proved, using theoretical calculations, the role of pyridinium in the photocatalytic CO_2 reduction reaction. They showed that the adsorbed species could react to form adsorbed dihydropyridine, which was previously proposed to play the role of the active catalyst in this system.[51]

2.1.4 II–VI group photo-absorbers. Cadmium sulfide (CdS), a representative semiconductor of the II–VI group, has great potential in solar energy conversion due to its suitable band gap ($E_g = 2.4$ eV) and band energy levels. In the last ten years, different morphologies of CdS and CdS-based nanomaterials have been developed for photocatalytic CO_2 reduction.[52,53] However, the efficiency of pure CdS for the photocatalytic reduction of CO_2 is generally low due to its unstable photochemical properties, severe photo-corrosion, and rapid recombination of photogenerated electron–hole pairs.[59] Constructing heterojunctions, like Z-scheme structures and metal-doping can alleviate photo-induced electron–hole recombination and enhance the photocatalytic activity of the

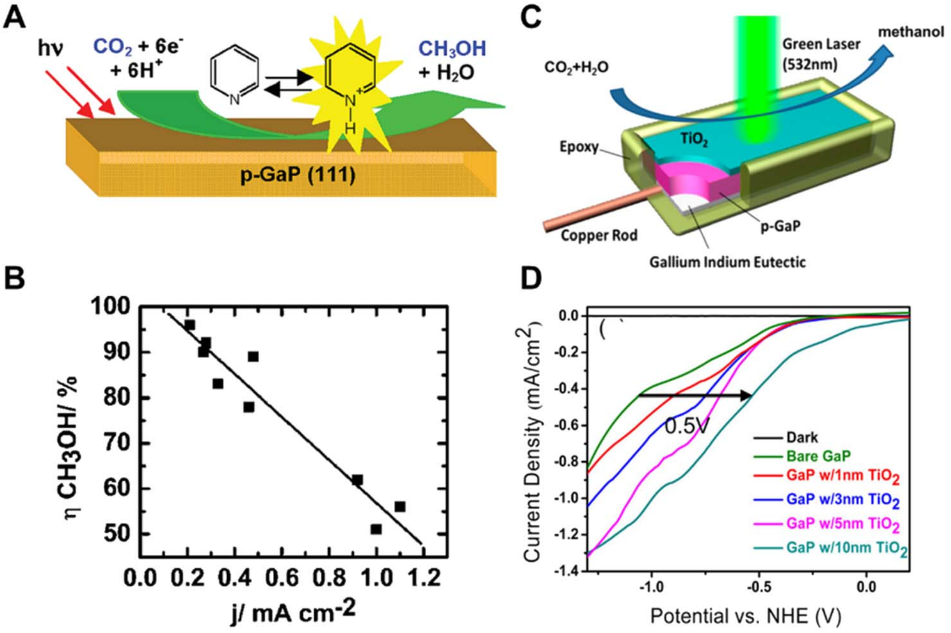

Fig. 6 (A) Schematic of pyridinium ion catalyst decorated p-GaP for CO_2 reduction, (B) relationship of increasing methanol yield with decreasing current density.[49] Copyright 2008, American Chemical Society. (C) Schematic of TiO_2 passivated GaP photocathodes in photocatalytic CO_2 reduction under 532 nm wavelength laser illumination, (D) photocatalytic current–potential curves of GaP photocatalysts with different TiO_2 thicknesses in a 0.5 M NaCl, 10 mM pyridine solution under 532 nm wavelength laser illumination.[50] Copyright 2014, American Chemical Society.

material. Yu *et al.* reported a TiO_2/CdS Z-scheme system.[54] The optimized photocatalytic CO_2 reduction performance of TiO_2/CdS was 3.5, 5.4, and 6.3 times higher than that of CdS, TiO_2, and commercial TiO_2 (P25), respectively. Hou *et al.* prepared an Ag–CdS nanocomposite by photo-deposition, which produced 3 times the amount of CO than that obtained with untreated CdS.[55] Ag served as the electron trap and active sites for CO_2 reduction in this Ag/CdS system, which enhanced the activity and selectivity of CO_2 to CO.

2.1.5 Perovskite materials.

Lead halide perovskites have recently emerged as promising light absorbers for solar fuel conversion and they can either be integrated as an encapsulated component in a photoelectrochemical (PEC) device, which will be further discussed in Section 3.2, or coupled as external photovoltaic cells to an electrolyzer (PV-EC).[56] In 2015, Grätzel *et al.* constructed a PV-EC system composed of three series-connected perovskite photovoltaics and a high-performance electrolyzer with Au as the catalytic electrode (Fig. 7A–C), reaching a solar-to-CO efficiency exceeding 6.5%.[57] The study represented one of the first extended demonstrations, showing the stable operation of perovskite photovoltaics, whose large photovoltage was found to be particularly suited to this process.

Apart from their use as a PV cell, the lead halide perovskites are also attractive semiconductor compounds for photocatalytic CO_2 reduction due to their suitable bandgap, conduction and valence band levels.[59] In 2017, Kuang's group first reported the artificial photosynthesis based on halide perovskite QDs for CO_2 reduction in non-aqueous media.[60] Under AM 1.5G simulated illumination, the $CsPbBr_3$ QD/graphene oxide ($CsPbBr_3$ QD/GO) composite catalyzed CO_2 reduction into CO and CH_4 with a selectivity over 99.1%. Afterwards, they further investigated a Pt decorated $CsPbBr_3$ perovskite for photocatalytic CO_2 reduction in non-aqueous solvents.[61] The previous studies on perovskites as photocatalysts to convert CO_2 into solar fuels were commonly carried out in non-aqueous media due to the water sensitivity of perovskites. To improve the water stability of perovskites, strategies for preventing the contact of perovskites with water were commonly adopted. Lu *et al.* encapsulated low-cost $CH_3NH_3PbI_3$ ($MAPbI_3$) perovskite QDs in the pores of Fe porphyrin MOF (PCN-221(Fe_x)) and obtained an enhanced catalytic performance and stability with water as the electron donor for photocatalytic CO_2 reduction (Fig. 7D–F).[58] Coating a thin graphdiyne layer on $CsPbBr_3$ nanocrystals also delivered a significant improvement in stability for CO_2 reduction in an aqueous system.[62] It is worth noting that an isotopic labeling test using $^{13}CO_2$ must be carried out for experiments involving organic media as the solvent. This is to confirm that the CO_2 reduction products are indeed derived from CO_2. To increase the application of perovskite materials, more practical hydrophobic treatments and encapsulation techniques are required. The relationship between photocatalytic activity and crystal structure, and the behavior of the photoelectrons at the surface should be further investigated to develop more efficient perovskite materials. In addition, new water stable perovskites are demanded.

2.1.6 Carbon nitrides.

As a series of photocatalysts, polymeric carbon nitrides (PCNs) have advantages such as sustainability,[63] facile synthesis and optimization[64] and reliability, but the range of visible light absorption of PCNs is mainly concentrated in the blue to violet light region, resulting

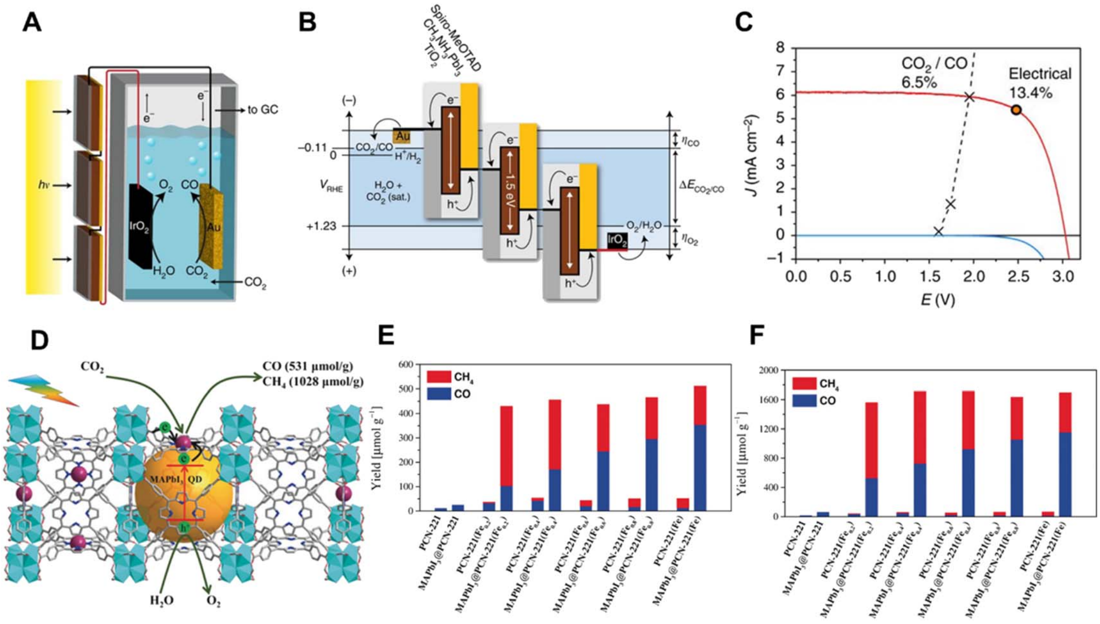

Fig. 7 (A) Schematic illustration of the device combining photovoltaics with an electrochemical cell. (B) Generalized energy diagram for converting CO_2 into CO with three perovskite solar cells connected in series, (C) *J*–*V* curves of three series-connected perovskite cells under simulated AM 1.5G 1 Sun solar irradiation and in the dark, overlaid with the matched *J*–*V* characteristic of the CO_2-reduction and oxygen-evolution electrodes. The maximum power point of the photovoltaics is indicated by the circled red dot on the curve.[57] Copyright 2015, Springer Nature. (D) Schematic diagram of CO_2 photoreduction over the $MAPbI_3$@PCN-221($Fe_{0.2}$) photocatalyst, photocatalytic performance: yield of the CO_2 reduction to CH_4 and CO in the CO_2-saturated ethyl acetate/water solution after (E) 25 h and (F) 80 h.[58] Copyright 2019, Wiley.

in a low visible-light photocatalytic efficiency.[65] The investigation of pristine PCNs for CO_2 reduction was first presented by Zhang and Dong in 2012.[66] They used melamine and melamine hydrochloride as the precursors to synthesize PCN for the reduction of CO_2 to CO under visible light illumination. In 2013, Peng and co-workers prepared PCN derived from urea and melamine with different morphologies.[67] A mesoporous flake-like structure and a non-porous flaky structure were compared for photocatalytic CO_2 reduction in an aqueous system under visible light irradiation. The materials exhibited different selectivities for the formation of CH_3OH and C_2H_5OH. Furthermore, different metal-free (S, P, B or halogen doped) PCNs were investigated for photocatalytic CO_2 reduction. Sulfur-doped g-C_3N_4 was found to absorb light up to 475 nm corresponding to a band gap of 2.63 eV, which was narrower than that of undoped g-C_3N_4 with a band gap of 2.7 eV and the CH_3OH yields were 1.12 and 0.81 mol g^{-1}, respectively, under UV-vis light irradiation.[68]

On the other hand, PCN materials have emerged as promising cheap and benign semiconductors for PEC cells during the last decade, owing to their stability under harsh conditions and suitable energy band edges for water-splitting and other chemical transformations.[69] A thin film composed of g-C_3N_4 doped with or without boron atoms was fabricated using an electrophoresis deposition method, and it was found that the $BCN_{3.0}$ exhibited a higher CO_2 reduction activity owing to its suitable band edges.[70] Furthermore, cocatalysts, including Ag, Rh and Au were decorated on the surface of g-C_3N_4 and B-doped g-C_3N_4. The photocurrent of Rh–$BCN_{3.0}$ was approximately 10 times larger than that of the original g-C_3N_4, and the Au–$BCN_{3.0}$ produced more ethanol compared to the other electrodes. A type-II g-C_3N_4/ZnTe heterojunction was constructed by Wang and co-workers for photoelectrochemical CO_2 reduction and it was proven to possess an enhanced photo-generated electron–hole separation and efficient electron transfer from g-C_3N_4 to ZnTe.[71] The g-C_3N_4/ZnTe photocathode yielded an impressive ethanol generation rate of 17.1 μmol cm^{-2} h^{-1} at −1.1 V (*vs.* Ag/AgCl) in CO_2-saturated 0.1 M $KHCO_3$ aqueous solution under AM 1.5G illumination.

PCNs are promising photo-absorber materials due to their unique electronic structure and high stability against high temperature, acids, bases, and organic solvents. Further exploration into functionalized g-C_3N_4 with specific chemical groups and elemental doping may be practical approaches for extending their absorption in visible light range. Furthermore, it is important for the application of g-C_3N_4 as a photoelectrode by exploring thin film-formation methods and developing protection layers.

2.1.7 Metal organic frameworks and metal complexes. Metal organic frameworks (MOFs), as a class of 3D crystalline porous compounds, with metal ions/clusters as nodes and organic ligands as linkers,[72] are promising and tailorable materials for various fields ranging from energy storage, sensors, gas uptake and catalysis.[73,74] Benefiting from their excellent CO_2 adsorption capacity, adjustable light-harvesting ability, uniformly distributed catalytic active sites and adjustable high-density metal nodes, MOFs have been recommended as promising materials for photo-driven CO_2 reduction.[75–77]

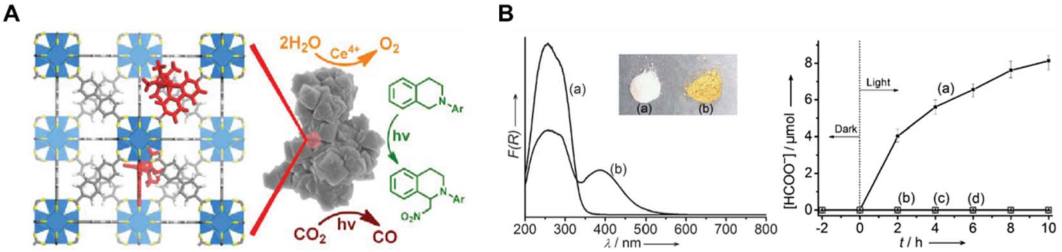

Fig. 8 (A) Schematic illustration of the MOF [Re^{I}(CO)$_3$(bpydc)Cl] for photocatalytic CO_2 reduction.[78] Copyright 2011, American Chemical Society. (B) (left) UV/Vis spectra (a) MIL-125(Ti) and (b) NH_2-MIL-125(Ti) and the inset shows a photo of the samples of the corresponding samples and (right) the amount of $HCOO^-$ produced as a function of the irradiation time.[79] Copyright 2012, Wiley.

However, not all MOFs are photoactive. According to their different functions in solar driven catalytic systems, MOFs can act as the photo-absorber, co-catalyst, or as both photo-absorber and co-catalyst.

Re(bpydc) $(CO)_3Cl$ complexes have been incorporated into UiO-67 MOF for photocatalytic CO_2 reduction, leading to high catalytic activity for the light-driven reduction of CO_2 to CO (Fig. 8A).[78] Inspired by this work, intensive research has been conducted on constructing photoactive MOFs for visible light-driven CO_2 reduction. Li *et al.* reported an amine-functionalized MOF, NH_2-MIL-125(Ti), which presented a broad absorption band and enhanced photocatalytic activity of CO_2 to $HCOO^-$ compared with MIL-125(Ti) (Fig. 8B).[79] In this titanium-based MOF, NH_2-BDC linkers absorbed light and generated photoelectrons, which were then transferred to the Ti centers (active sites for CO_2 reduction) by the ligand to metal charge transfer (LMCT) process. Porphyrin-incorporated MOF (PCN-222) was also proven to be a highly efficient photocatalyst for CO_2 reduction under visible-light irradiation.[80] PCN-222 was found to contain deep electron trap states, which inhibited electron–hole recombination and prolonged the lifetime of photo-excited electrons.

By far, plenty of strategies have been adopted to achieve highly active photo-driven CO_2 reduction using MOF-based materials.[81] The methods of designing highly active MOF composites include improving the visible-light absorption and the charge-carrier separation.[82] Adjusting organic ligands and functionalization of metal centers are common strategies for enhancing visible-light absorption and charge-carrier separation.[82,83]

2.2 Catalysts

In PC, PEC and PV-EC CO_2 reduction systems, catalysts are generally needed.[84,85] In the PC or PEC system, the photo-absorber may also act as the catalytically active ingredient, but the discussion in this part mainly focuses on the catalysts, which play a key role in improving the performance of photochemical CO_2 reduction systems. The catalysts can promote photochemical CO_2 reduction in the following ways: (i) by lowering the activation energy or overpotential required for CO_2 reduction, (ii) by promoting the separation and transport of photo-excited electron–hole pairs, (iii) by improving the stability of the photoelectrodes or photo-absorbers through rapidly transferring the surface charge carriers and (iv) by increasing the product selectivity through tuning the adsorption strengths of key reaction intermediates.[4,86]

Recently, there have been many well-designed electrocatalysts for electrocatalytic CO_2 reduction that have been adopted in solar driven CO_2 reduction systems. Driven by electricity, CO_2 is converted into carbonaceous products on the electrocatalysts. As shown in Table 1, the production of general C1–C3 products: CO/HCOOH, HCHO, CH_3OH, CH_4/CH_3COOH, CH_3CHO, C_2H_5OH/C_2H_4, C_2H_6, C_2H_5CHO and C_3H_7OH requires the consumption of 2, 4, 6, 8, 10, 12, 14, 16 and 18 electrons, respectively.[87] Although the equilibrium potentials of CO_2 reduction are all close to 0 V *vs.* RHE, the overpotentials required are still high due to the reaction barriers. In addition, the similar equilibrium potentials of the various half-reactions of CO_2 reduction and the competing hydrogen evolution reaction (HER) lead to a low target product selectivity of CO_2 reduction. Hence, catalysts that facilitate the reaction kinetics and enhance the product selectivity are required. The most investigated materials are metal-based catalysts, which are widely studied from the aspect of geometric structures, compositional survey, mixing patterns of constituent metals, oxidation states, coordination structure and defect engineering to improve catalytic activity and product selectivity. Metal-free and hybrid catalysts, like bacteria and the hybrid materials combining bacteria and metals have also been used for electrocatalytic CO_2 reduction. Over the past few decades, CO_2 reduction electrocatalysts have been well studied and milestones have been achieved. Catalysts that convert CO_2 into C1 products with FE close to 100% were reported in recent years.[88–92] In another study, a FE of 85% for CH_4 was also achieved on a single-atom Zn catalyst.[93] Huang *et al.* reported copper nanowires with rich surface steps which converted CO_2 into C_2H_4 with a FE of more than 70% over 200 h.[94] Recently, long-chain C3 to C6 hydrocarbons were produced with a sustained FE of up to 6.5% using polarized nickel catalysts.[95]

The well-designed CO_2 reduction electrocatalysts promote the rapid development of catalysts for solar driven CO_2 reduction. Metal-based catalysts (including mono-metals,[96] bimetals,[89,97] metal oxides,[98] metal sulfides,[99] metal carbides[100]) and biomimicking catalysts[101] are commonly studied catalysts.

2.2.1 Metal-based catalysts.

Mono-metals are the most commonly studied metal catalysts. Previously, Hori has

Table 1 Equilibrium potentials of commonly reported CO_2R reactions and corresponding electrochemical products.[10] Copyright 2019, American Chemical Society

Reaction	Product	Number of electrons transferred	Equilibrium potentials (V *vs.* RHE)
CO_2R	CO (g)	2	−0.10
	HCOOH (aq)	2	−0.12
	HCHO	4	−0.09
	CH_3OH (aq)	6	0.03
	CH_4 (g)	8	0.17
	CH_3COOH (aq)	8	0.11
	CH_3CHO (aq)	10	0.06
	C_2H_5OH (aq)	12	0.09
	C_2H_4 (g)	12	0.08
	C_2H_6 (g)	14	0.14
	C_2H_5CHO (aq)	16	0.09
	C_3H_7OH (aq)	18	0.10
HER	H_2	2	0

classified metal catalysts into four different groups based on their main product selectivity in electrochemical CO_2 reduction:[102] (i) H_2 selective metals, such as Ti, Fe, Ni, Pt, Pd and Ga, (ii) CO selective metals, including Au, Ag and Zn,[90] (iii) formate selective metals, such as Cd, Hg, In and Sn, (iv) Cu, a unique mono-metal which can reduce CO_2 into hydrocarbons, alcohols and C2+ products.[103,104] Metals with high selectivity to certain CO_2 reduction products are also attractive when utilized as catalysts in solar driven CO_2 reduction systems.

Li *et al.* prepared a Si/Ag photocathode by controllable chemical etching on a Si wafer by Ag^+ ions (Fig. 9A).[105] The resultant photocathode exhibited a large photocurrent density of -10 mA cm^{-2} under 0.5 Sun illumination (Fig. 9B), an excellent CO faradaic efficiency of 90% at −0.5 V *versus* the reversible hydrogen electrode (Fig. 9C) and an operational stability exceeding 12 h. Photoelectrochemical CO_2 reduction to methanol, over a TiO_2-passivated InP nanopillar photocathode, was greatly enhanced after the deposition of Cu NPs (Fig. 9D and E).[106] To combine the catalytic effect and plasmonic effect of Au, Atwater *et al.* fabricated a gold/p-type gallium nitride (Au/p-GaN) Schottky junction tailored for photoelectrochemical

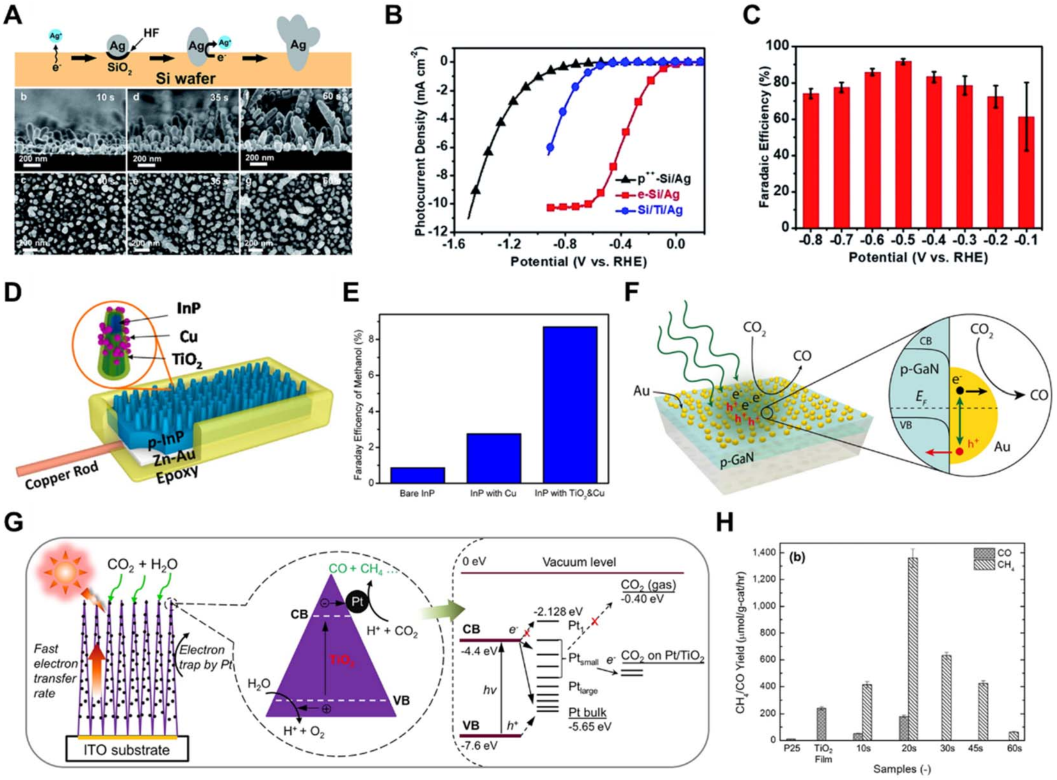

Fig. 9 (A) Schematic illustration of how a Si/Ag photocathode is prepared by controllable chemical etching on a Si wafer by Ag^+ ions (top) and SEM images of the Si/Ag photocathode preparation over time (bottom), (B) photocurrent density of the Si/Ag photocathode under 0.5 Sun illumination, (C) FE of the Si/Ag photocathode under 0.5 Sun illumination.[105] Copyright 2018, Royal Society of Chemistry. (D) Schematic illustration of a TiO_2-passivated InP nanopillar photocathode decorated with Cu NPs, (E) FE of a TiO_2-passivated InP nanopillar photocathode and control samples.[106] Copyright 2015, American Chemical Society. (F) Schematic illustration of gold/p-type gallium nitride (Au/p-GaN) Schottky junctions tailored for photoelectrochemical studies of plasmon-induced hot-hole capture and conversion.[107] Copyright 2017, American Chemical Society. (G) Schematic diagram of the CO_2 photoreduction mechanism by using Pt–TiO_2 nanostructured films, (H) CO and CH_4 yields of commercially available TiO_2 powders (P25), pristine TiO_2 columnar films (TiO_2 film), and Pt–TiO_2 films with different Pt deposition times.[109] Copyright 2012, American Chemical Society.

studies involving plasmon-induced hot-hole capture and conversion.[107] On the plasmonic Au/p-GaN photocathodes, hot holes from Au nanoparticles were injected into p-GaN upon plasmon excitation, since the vast majority of hot holes generated *via* interband transitions in Au were sufficiently hot to inject above the 1.1 eV interfacial Schottky barrier at the Au/p-GaN heterojunction (Fig. 9F).

In PC CO_2 reduction systems, metal co-catalysts, including Pt,[108–110] Ag,[111,112] Pd,[113,114] Ru,[115] Au[116] and others, have been more widely studied. A platinized titanium dioxide (Pt–TiO_2) nanostructured film was constructed based on unique one-dimensional (1D) columnar TiO_2 single crystals coated with ultrafine 0.5–2 nm Pt nanoparticles (Fig. 9G).[109] The Pt NPs improved the electron–hole pair separation and the electron-transfer rate in TiO_2 single crystals, which enhanced the amount of photocatalytic CO_2 reduction to CH_4 with a maximum yield of 1361 $\mu mol\ g_{cat}^{-1}\ h^{-1}$ (Fig. 9H). Therefore, in some cases metals functioning as catalysts in photochemical CO_2 reduction systems do not always display the same product selectivity as when they are used for electrochemical CO_2 reduction,[109] the mechanism of which needs further investigation.

It is important to note that bimetallic catalysts sometimes exhibit better catalytic activity for CO_2 reduction than monometals,[19] and the cost of the noble metal catalysts can be reduced by alloying noble metals with non-noble metals.[86] Yang *et al.* created an integrated photoelectrode by directly assembling Au_3Cu alloy NPs on TiO_2-protected n^+p-Si NW arrays (Fig. 10A).[117] Well-dispersed Au_3Cu NPs decorated Si NW arrays served as an effective CO_2 reduction photoelectrode, exhibiting a high CO_2-to-CO selectivity close to 80% at −0.20 V *vs.* RHE and remained stable for up to 18 h (Fig. 10B and C). A high-rate sunlight-driven conversion of diluted CO_2 to hydrocarbons was achieved by constructing a Cu–Pt inner coating and modulated-diameter TiO_2 nanotube photocatalyst.[118] As illustrated in Fig. 10D and E, the core–shell nanotube arrays with the inner walls of the double-walled TiO_2 nanotubes coated with bimetallic $Cu_{0.33}$–$Pt_{0.67}$ generated light hydrocarbons from low concentration CO_2 at room temperature.

In addition to monometals and bimetals, metal oxides, metal sulfides and metal carbides have also been utilized as co-catalysts in solar driven CO_2 reduction systems. A mixed-phase material consisting of $CuFeO_2$ and CuO was prepared by cathodic deposition on FTO substrates (Fig. 11A), and was employed as the photoelectrocatalyst in a PEC CO_2 reduction system.[119] The selectivity of the CO_2 reduction products could be adjusted from primarily acetate to primarily formate by varying the Fe : Cu atomic ratio from 1.3 to 0.1 (Fig. 11B and C). Purging with H_2S gas led to a spontaneous transformation of Cu to CuS, which presented a high FE of HCOOH.[120] Inspired by this work, Mi *et al.* prepared a Cu/GaN/Si photocathode,[121] and converted it into CuS/GaN/Si by exposing Cu/GaN/Si to an industrial CO_2 gas environment (contaminated with H_2S) during CO_2 reduction. The CuS-decorated GaN/Si photocathode exhibited a superior FE of 70.2% for formate and partial current density of 7.07 mA cm^{-2} at −1.0 V *vs.* RHE under AM 1.5G illumination (Fig. 11D). In PC CO_2 reduction systems, metal oxides, metal sulfides and metal carbides were studied more extensively as co-

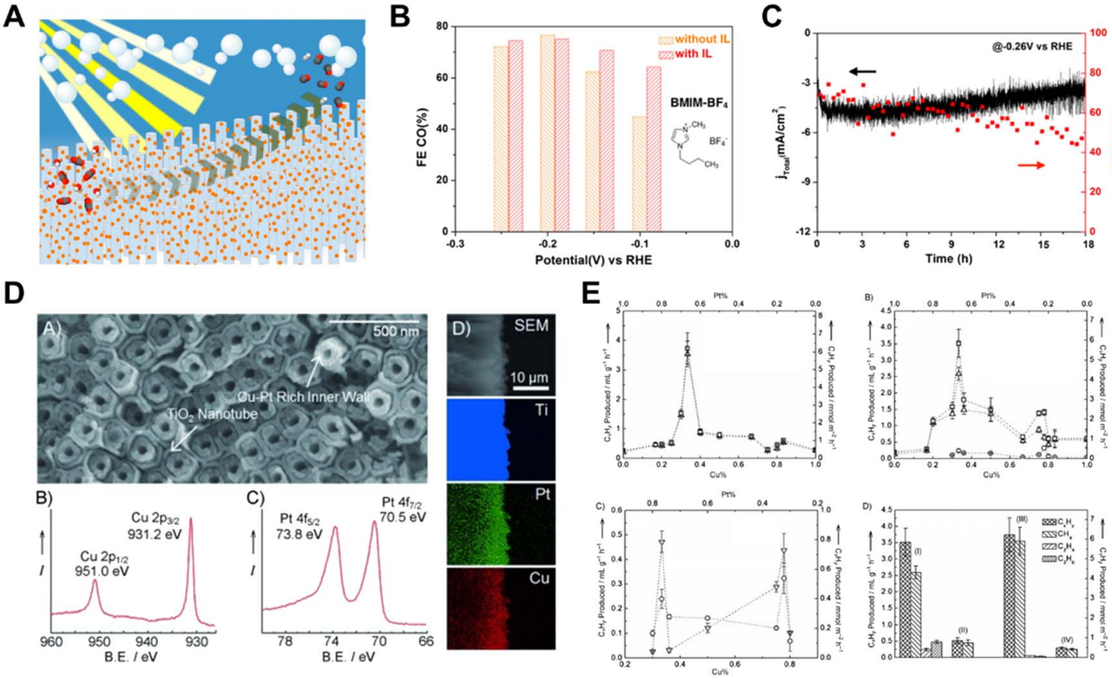

Fig. 10 (A) Schematic illustration of Au_3Cu alloy NPs on TiO_2-protected n + p-Si NW arrays, (B) and (C) FE and current density of hybrid Si NW arrays, respectively.[117] Copyright 2016, American Chemical Society. (D) SEM image and XPS spectra of core–shell nanotubes with bimetallic $Cu_{0.33}$–$Pt_{0.67}$ coating on the inner walls of the double-walled TiO_2 nanotube arrays, (E) CO_2 conversion performance of core–shell nanotubes with bimetallic $Cu_{0.33}$–$Pt_{0.67}$ coating on the inner walls of the double-walled TiO_2 nanotube arrays.[118] Copyright 2012, Wiley.

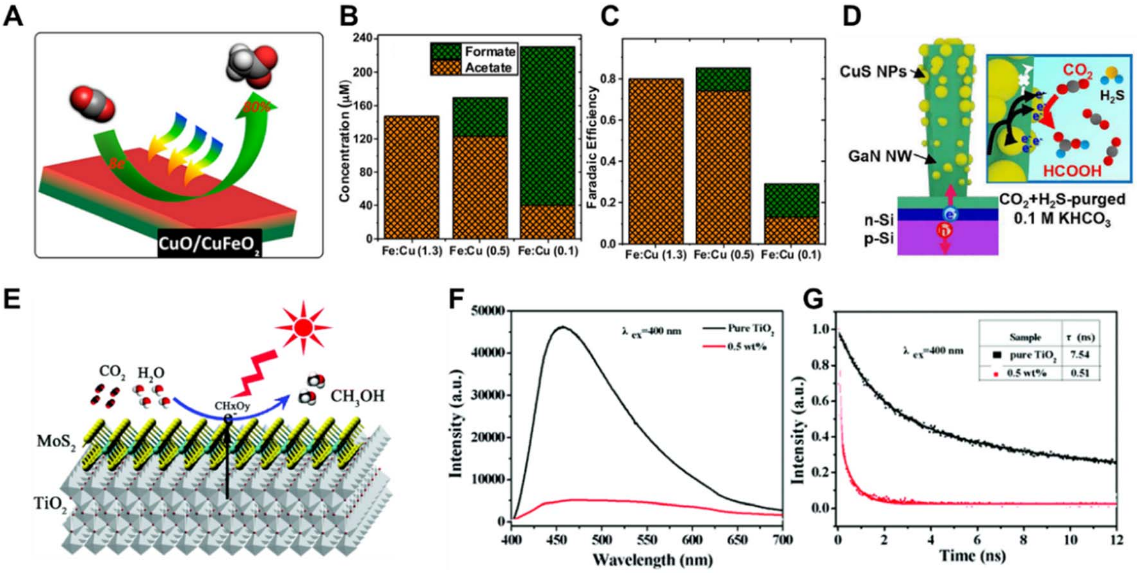

Fig. 11 (A) Schematic illustration of a mixed-phase material consisting of $CuFeO_2$ and CuO for CO_2 conversion, (B) and (C) CO_2 reduction performance according to the ratio of Fe and Cu.[119] Copyright 2017, American Chemical Society. (D) Schematic illustration of the CuS-decorated GaN/Si photocathode for CO_2 reduction.[121] Copyright 2021, American Chemical Society. (E) Schematic illustration of two-dimensional MoS_2–TiO_2 hybrid nanosheets, (F) PL emission spectra of MoS_2–TiO_2 hybrid nanosheets, (G) normalized TRPL decay traces of MoS_2–TiO_2 hybrid nanosheets.[123] Copyright 2017, Royal Society of Chemistry.

catalysts. RuO_2 loaded mesoporous $ZnGa_2O_4$ exhibited a high photocatalytic activity for converting CO_2 into CH_4 under light irradiation.[122] The two-dimensional MoS_2–TiO_2 hybrid nanosheet (Fig. 11E) performed an enhanced photocatalytic reduction of CO_2 to methanol.[123] As demonstrated by the photoluminescence (PL) emission spectra and normalized time-resolved photoluminescence (TRPL) decay traces (Fig. 11F and G), the MoS_2-loaded TiO_2 nanosheets promoted the electron transfer from TiO_2 to MoS_2 and minimized charge carrier recombination, improving the conversion efficiency of the photoreduction of CO_2 to CH_3OH. However, the real active sites during the catalytic reaction on the co-catalysts of metal oxides and metal sulfides should be studied by *in situ* and *operando* physical and chemical characterizations, since most of the metal oxides and metal sulfides are not stable under reduction conditions.

2.2.2 **Biomimicking catalysts.** Apart from the aforementioned metal-based active ingredients, some biological materials, such as enzyme biocatalysts[124] and bacterial catalysts[101] are also adopted in photochemical CO_2 reduction systems by coupling them with photo-absorbers.[125] These materials are mainly studied in PEC and PC CO_2 reduction systems. Yang *et al.* systematically investigated the correlation between a bioinorganic interface and the CO_2-conversion efficiency by constructing a silicon nanowire/*Sporomusa ovata* system (Fig. 12A).[126] By tuning the bulk electrolyte pH and increasing its buffering capacity, they obtained a close-packed nanowire–bacteria photocathode, which achieved a CO_2 reduction current density of $\sim$0.65 mA cm^{-2} and a solar-to-acetate production efficiency of $\sim$3.6% over 7 days. In PC CO_2 reduction systems, enzymes and bacteria are also utilized as catalysts by combining them with photo-absorbers to improve the catalytic performance. A hybrid enzyme–nanoparticle system consisting of RuP-sensitized TiO_2 nanoparticles and CODH I enzyme was reported by Armstrong *et al.* (Fig. 12B).[124] Enzyme CODH I served as the catalyst for CO_2 photoreduction and facilitated the production of CO with an average turnover rate of 250 μmol of CO (g of TiO_2)$^{-1}$ h^{-1} at pH 6 and 20 °C under visible light illumination. Combining the light harvesting ability of inorganic semiconductors with biocatalysts can also achieve highly efficient photoreduction of CO_2. Yang *et al.* integrated a non-photosynthetic bacterium with cadmium sulfide nanoparticles (Fig. 12C), which allowed continuous acetic acid production over several days of light–dark cycles,[101] demonstrating the capability of organism–semiconductor hybrid systems for photochemical CO_2 reduction. Recently, Reisner *et al.* reported a bio–abiotic hybrid system consisting of a semiconductor sheet and a non-photosynthetic CO_2-fixing acetogenic bacterium *Sporomusa ovata*, where the semiconductor sheet was La and Rh co-doped $SrTiO_3$ and Mo-doped $BiVO_4$ with Cr_2O_3/Ru as the co-catalyst for water reduction and RuO_2 as the co-catalyst for water oxidation (Cr_2O_3/Ru–$SrTiO_3$:La,Rh|ITO|RuO_2–$BiVO_4$:Mo), respectively (Fig. 12D).[127] The *S. ovata*|Cr_2O_3/Ru–$SrTiO_3$:La,Rh|ITO|RuO_2–$BiVO_4$:Mo hybrid converted CO_2 into CH_3COO^- with a production rate of $\sim$40 μmol cm^{-2} in 15 h under ambient conditions and 1 Sun illumination, achieving a solar-to-acetate conversion efficiency of 0.7%, and remained stable over 45 h (Fig. 12E). In summary, the hybrid photochemical CO_2 reduction system assisted by biological materials, such as enzymes and bacteria, enabled the production of C2/2+ products from CO_2 with high selectivity and stability.

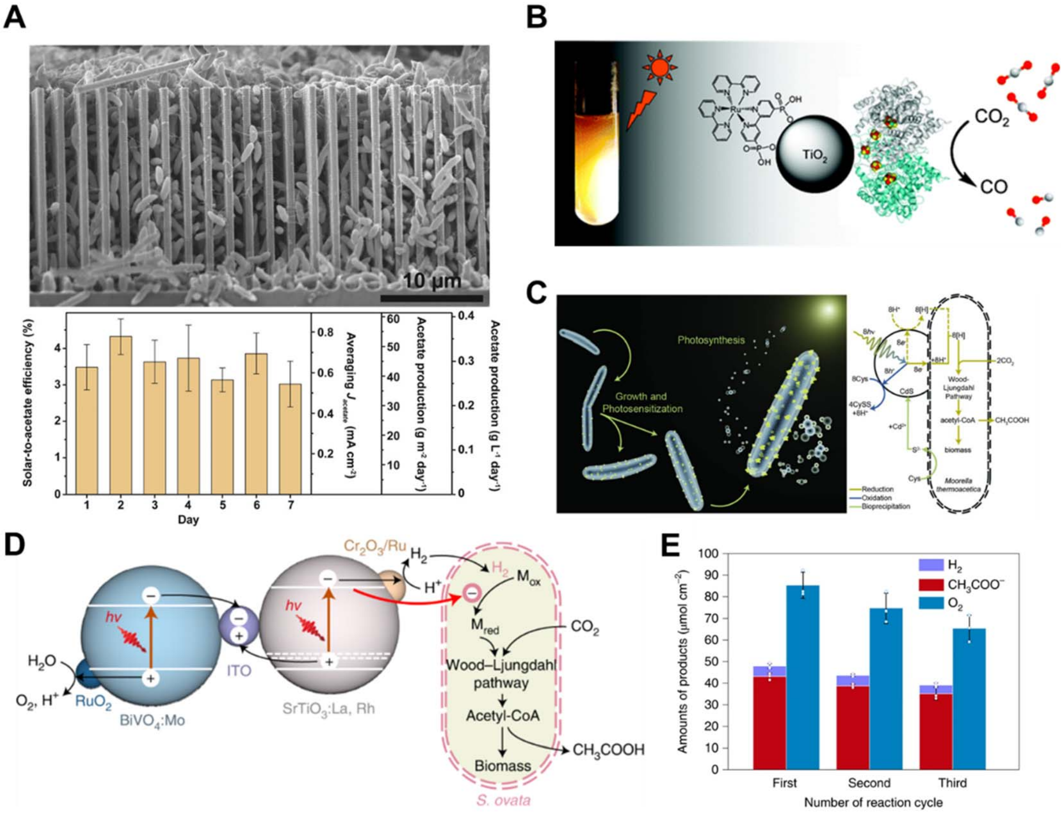

Fig. 12 (A) SEM image of the silicon nanowire/*Sporomusa ovata* system.[126] Copyright 2020, Elsevier. (B) Schematic illustration of a hybrid enzyme–nanoparticle system for CO_2 conversion.[124] Copyright 2010, American Chemical Society. (C) Schematic illustration of a non-photosynthetic bacterium integrated with cadmium sulfide nanoparticles for CO_2 conversion. Bacteria–photocatalyst hybrid system for CO_2 reduction.[101] Copyright 2016, American Association for the Advancement of Science. (D) Schematic illustration of the mechanistic pathway of photosynthetic CO_2-to-acetate conversion coupled with water oxidation over *S. ovata*|Cr_2O_3/Ru–$SrTiO_3$:La,Rh|ITO|RuO_2–$BiVO_4$:Mo, and (E) reduction products accumulation for three runs of 15 h, with reloading of Cr_2O_3 for every cycle.[127] Copyright 2022, Springer Nature.

The diverse electrocatalysts available for use in the EC system greatly promote the development of the PV-EC system, since almost all the electrocatalysts can also be utilized in the PV-EC system. Except for the co-catalysts mentioned above, Cu based catalysts have unparalleled selectivity for hydrocarbons and multi-carbon products and single atom catalysts show high selectivity towards C1 products. However, the selectivity of reduction products in the PV-EC system is also affected by the operating voltage of PV. To achieve a highly selective PV-EC system, the optimum output voltage of the PV needs to be compatible with the electrocatalysts.

3. Devices: progress and challenges

Highly efficient solar driven CO_2 reduction requires not only active materials for CO_2 conversion, but also a rationally designed device. A higher CO_2 conversion efficiency is achievable when the device has enhanced light absorption, improved mass transfer, optimal gaseous/liquid flow field management and the heat management from device engineering aspects.[128,129]

3.1 Recent progress of PC devices

The PC devices that are commonly in use are slurry photoreactors and fixed bed photoreactors.[129–131] According to the type of illumination method employed, the slurry photoreactors are further divided into externally illuminated and internally illuminated reactors.[132,133] The catalytic reactions carried out in slurry photoreactors involve a slow mass transfer of gas–liquid–solid triple-phase and the solubility of CO_2 in liquid is low, which limits the catalytic reaction rate. To simplify this process and improve the concentration of CO_2 in the catalyst surroundings, fixed bed photoreactors involving a two-phase, gas–solid catalytic reaction were developed.[134] In fixed bed photoreactors, the catalysts are fixed on various supports, such as glass,[135] monoliths[136] and packed beds.[137]

In a recent study, Cu_2O decorated reduced titania (RT) nanoparticles were packed to form a fixed bed in a continuous flow reactor (Fig. 13A).[137] In this system, the optimized RT-Cu_2O photocatalyst enabled CH_4 evolution with a yield of 462 nmol g^{-1} (Fig. 13B). The reaction was conducted using highly diluted CO_2 in water vapor under illumination for 6 h, and it exhibited excellent stability over seven testing cycles (42 h). The direct Z-scheme charge transfer mechanism taking place across a well-

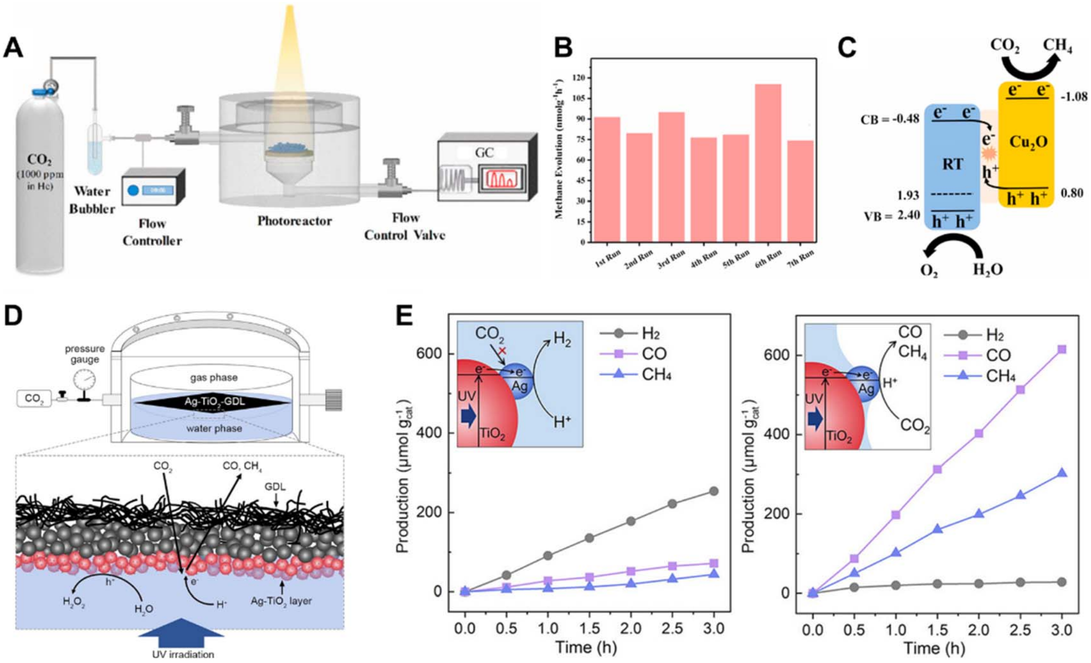

Fig. 13 (A) Schematic illustration of the experimental setup for photocatalytic CO_2 reduction involving a fixed bed of Cu_2O decorated RT nanoparticles, (B) CH_4 evolution rate over seven sequential 6 h tests of the optimized RT-$Cu_{0.75}$ sample, (C) energy band alignment (in V *vs.* NHE at pH = 7), charge transfer and reaction mechanism for the described RT-Cu_2O Z-scheme showing CO_2 + H_2O into CH_4 transformation.[137] Copyright 2020, Elsevier. (D) Schematic illustration of the tri-phase photocatalytic CO_2RR system based on Ag–TiO_2 supported at the gas–water boundary, (E) time-dependent CO_2RR over Ag–TiO_2 NPs in the water phase (left) and supported at the gas–water boundary (right). Insets schematically illustrate the photocatalytic processes of the two systems.[138] Copyright 2022, Wiley.

designed interface inhibited the photo-corrosion of Cu_2O (Fig. 13C). This coupled with the packed bed flow reactor synergistically enabled the excellent stability. Zhang *et al.* set up a photoreactor which enabled a triple-phase photocatalytic CO_2RR reaching a high CO_2 reduction rate of 305.7 μmol g^{-1} h^{-1}, which was approximately 8 times higher than that of the bi-phase system.[138] The Ag decorated TiO_2 supported on a gas diffusion layer (GDL) formed a triple-phase at the gas–water boundary (Fig. 13D), which greatly promoted the mass transfer of CO_2 (Fig. 13E). Therefore, the triple-phase photocatalytic CO_2RR system exhibited a high CO_2 reduction performance.

3.2 Recent progress of PEC devices

The H-type photo-electrolyzer has received the most practical lab use in the PEC system and the batch mode is the most common operation mode, in which the products can be accumulated for detection (Fig. 14A). However, the mass transfer limitation and the low CO_2 solubility in aqueous solution promote the upgrading of the H-type photo-electrolyzer. Therefore, continuous flow PEC reactor (CFPR) devices have been developed for PEC CO_2 reduction.[139] With a hybrid p-type CuO/Cu_2O semiconductor nanorod array as the photocathode, the flow system exhibited a high activity for producing alcohols (ethanol and isopropanol) with a liquid alcohol production rate of 0.22 ml m^{-2} h^{-1}, which was approximately 6 times higher than the production rate of a batch mode electrolyzer design. The photocurrent density was significantly enhanced in the CFPR, benefiting from its high surface area-to-volume ratio provided by the narrow reaction channels (Fig. 14B). To highlight the significance of the reactor design, Andresen *et al.* constructed a continuous flow microfluidic PEC reactor with an α-Fe_2O_3/CuO thin film as the photocathode.[140] The sandwich-type planar microfluidic photo-reactor was a one chamber reactor constituting an α-Fe_2O_3/CuO/FTO photocathode, Pt/FTO anode, laser cut PMMA parts and Surlyn gaskets without any separator between the electrodes (Fig. 14C). Under backside AM 1.5 solar irradiation, the microfluidic system converted CO_2 to formate with an STF efficiency of 0.2% after 12 h illumination. Compared with the batch reactor, the continuous flow microfluidic PEC reactor promoted the formation of methanol.

In recent years, Reisner *et al.* constructed a series of highly integrated PV-PEC systems for CO_2 reduction. By immobilizing a cobalt porphyrin catalyst on carbon nanotubes with triple-cation mixed halide perovskite and $BiVO_4$ photoabsorbers, they demonstrated a highly tunable perovskite-$BiVO_4$ tandem PV-PEC syngas production system (Fig. 15A).[21] The tandem photocathodes exhibited a different syngas production ratio under different light intensities (Fig. 15B) for aqueous CO_2 reduction and maintained one day continuous syngas production at a light intensity of 0.1 Sun (Fig. 15C). They further fabricated a lightweight perovskite-$BiVO_4$ device with flexible substrates and carbonaceous protection layers.[142] A wired floating Ti|$BiVO_4$|TiCo-fPVK|GE|CoMTPP@CNT device was constructed by attaching a flexible perovskite photocathode (fPVK) with CoMTPP@CNT as the CO_2 reduction catalyst. The $BiVO_4$ photoanode was spin-coated with $TiCoO_x$ (TiCo) mixed with a contact adhesive, as

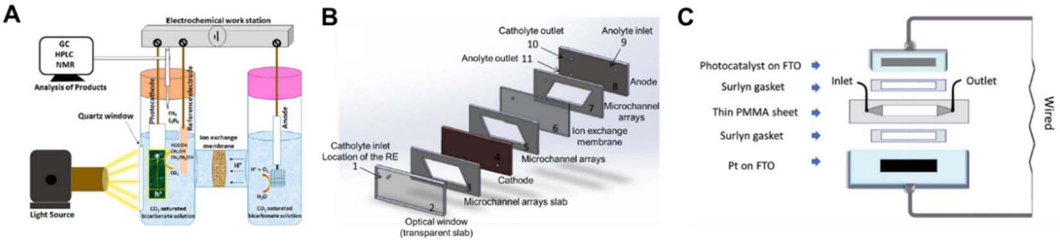

Fig. 14 Schematic diagrams of PEC devices for CO_2 conversion. (A) H-type PEC reactor.[141] Copyright 2020, American Chemical Society. (B) Continuous flow PEC reactor.[139] Copyright 2015, IOP Publishing. (C) Wired sandwich-type microfluidic PEC cell.[140] Copyright 2019, Royal Society of Chemistry.

the O_2 evolution catalyst (Fig. 15D). With an active light irradiation area of 1.7 cm^2, the Ti|BiVO$_4$|TiCo-fPVK|GE|CoMTPP@CNT device achieved a STF efficiency of 0.053 ± 0.006% (CO) and 0.021 ± 0.004% (H_2), as demonstrated in Fig. 15E. The impressive scalable integrated PV-PC device opens a new prospect for the application of solar driven CO_2 reduction.

As one of the key components, ion exchange membranes also play a key role in improving the performance of the photoelectrolyzer. Compared with anion exchange membranes, proton exchange membranes (PEMs) are preferred in H-type PEC devices with 0.1 M $KHCO_3$ as the electrolyte, owing to their ability to allow proton transportation from the anode to the cathode.[143] Recently, bipolar membranes (BPMs), which combine the characteristics of cation and anion exchange membranes, have gained great attention. Their high pH sensitivity enables the selective transport of OH^- to the anode and H^+ to the cathode under different electrolyte conditions.[143–145] Xiang *et al.* constructed a solar driven CO_2 reduction system with a TiO_2 protected III–V tandem photoanode in conjunction with a bipolar membrane and a Pd/C cathode.[145] Adopting two electrolytes with different bulk pHs, the bipolar membrane maintained a steady-state operation of the system, and the system achieved a CO_2 to HCOOH FE > 94% (8.5 mA cm^{-2}) and a ∼10% solar-to-fuel conversion efficiency.

3.3 Recent progress of PV-EC devices

The key aspects to make an efficient PV-EC CO_2 reduction device are decreasing the reaction energy barriers, minimizing the electrical energy losses and tuning the selectivity of the desired products.[146] The research on PV-EC for CO_2 reduction has demonstrated higher STF efficiencies than PC and PEC devices,[18,147–149] suggesting that it is a promising technology for direct CO_2 conversion using solar energy.

Morikawa *et al.* reported a monolithic tablet-shaped device with a solar-to-chemical energy conversion efficiency of 4.6% for CO_2 photoreduction to formate by utilizing water as an electron

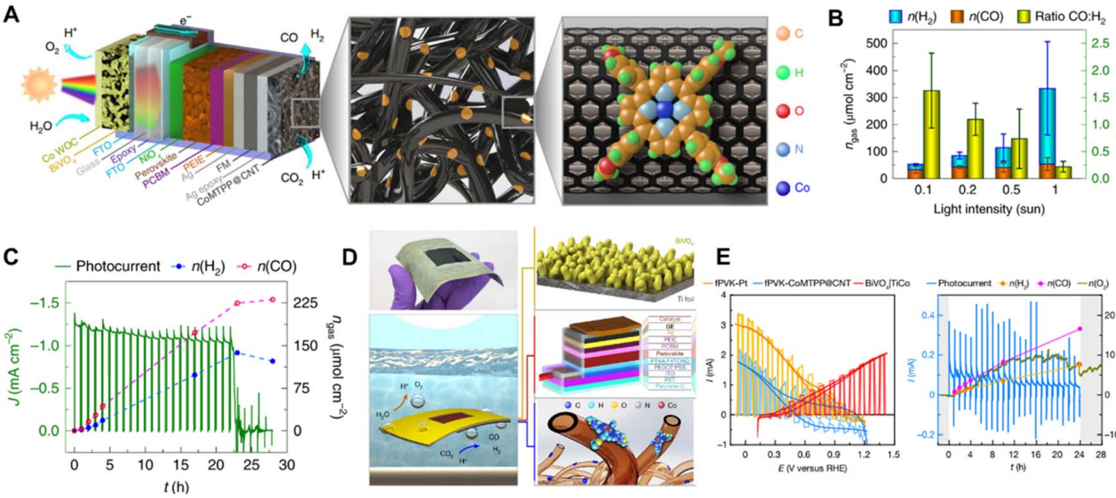

Fig. 15 (A) Schematic illustration showing the architecture of the standalone perovskite–BiVO$_4$ PEC tandem device for bias-free syngas production, (B) amounts of products produced and CO:H_2 selectivity after 4 h irradiation with different light intensities, (C) stability test under 0.1 Sun irradiation and the corresponding product amounts.[21] Copyright 2020, Springer Nature. (D) Photo of the actual lightweight floating perovskite-BiVO$_4$ device (top) schematic illustration of the floating perovskite-BiVO$_4$ device showing the concurrent water-splitting and CO_2 reduction reactions taking place (bottom), (E) photoelectrochemical performance of the floating perovskite-BiVO$_4$ devices: CVs of small-scale individual perovskite and BiVO$_4$ photoelectrodes assembled in a 1.7 cm^2 wired PEC device (left), chronoamperometric trace and amounts of products obtained for a 1.7 cm^2 wired perovskite-BiVO$_4$ device with a CoMTPP@CNT catalyst over 24 h at zero applied bias voltage (right).[142] Copyright 2022, Springer Nature.

donor under simulated solar light irradiation.[150] In the monolithic tablet-shaped PV-EC device, a triple-junction of amorphous silicon–germanium (SiGe-jn) functionalizing as the PV, converted solar energy into electricity and powered the catalytic reaction. Concurrently, the porous ruthenium complex polymer (p-RuCP) as the CO_2 reduction catalyst and iridium oxide (IrO_x) as the water oxidation catalyst reduced CO_2 into formate and oxidized water into O_2, respectively (Fig. 16A). Different from the monolithic device, the Ager group used a four-terminal III–V/Si tandem solar cell configuration coupled with a nanostructured Cu–Ag bimetallic cathode (Fig. 16B), which yielded a solar conversion efficiency to hydrocarbons and oxygenates exceeding 5% under 1 Sun illumination (Fig. 16C).[151] The Gratzel group constructed a more efficient device with an atomic layer deposited SnO_2 on CuO nanowires as the cathode and a GaInP/GaInAs/Ge cell as the photovoltaic (Fig. 16D), producing a peak solar-to-CO conversion efficiency of 13.4% (Fig. 16E).[13] In that work, the energy loss was minimized by matching the current density of the photovoltaic with the cathode catalyst. Recently, they also reported a solar driven CO_2 reduction system which coupled a flow cell composed of a tin oxide surface dominant copper/tin-oxide catalyst with a III–V triple junction solar cell, reaching a solar-to chemical energy conversion efficiency approaching 20%.[152] To further improve the STF efficiency of the PV-EC device, Salehi-Khojin *et al.* constructed a one compartment electrochemical flow cell consisting of a MoS_2 nanoflakes (NFs)/GDL cathode and an IrO_2 nanopowder/GDL anode.[153] By modifying the catalyst and adjusting the electrolyte, the PV-EC device composed of the flow

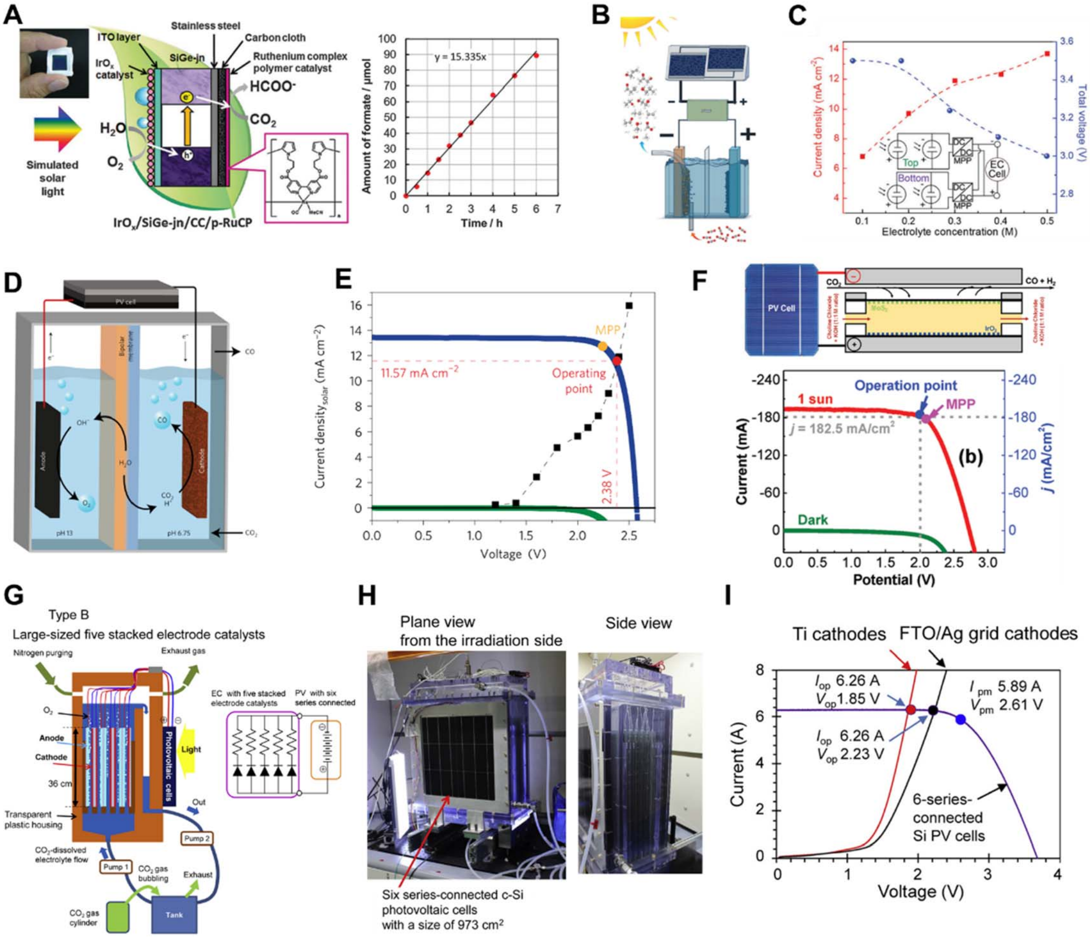

Fig. 16 (A) Schematic illustration of the monolithic tablet-shaped PV-EC device.[150] Copyright 2015, Royal Society of Chemistry. (B) Solar driven CO_2 RR measurements performed in a two-electrode configuration with a CuAg nanocoral cathode and an IrO_2 nanotube anode in tandem with two series-connected solar cells and a maximum power point (MPP) tracker, (C) measured current density (left axis, red) and voltage (right axis, blue) of PV-EC (PV was two tandem cells connected in parallel) as a function of electrolyte concentration at 1 Sun illumination. Inset depicts the circuit diagram.[151] Copyright 2017, Royal Society of Chemistry. (D) Schematic illustration of the device combining series-connected photovoltaics with an electrochemical cell, (E) photovoltaic and electrocatalytic *J*–*V* behaviours of the series-connected photovoltaic-electrochemical cell.[13] Copyright 2017, Springer Nature. (F) Schematic illustration of the flow cell using solar energy to drive CO_2 reduction reaction and photovoltaic and electrocatalytic *J*–*V* curves.[153] Copyright 2019, Wiley. (G) Schematic illustration of large-sized cell with stacked electrode catalysts, (H) photographs of the large cell for solar driven CO_2 conversion with stacked electrode catalysts, (I) LSV curves of the large cells equipped with the stacked FTO/Ag grid cathodes and Ti cathodes, and current (*I*)–voltage (*V*) characteristics of the six series-connected c-Si-PV cells under the AM 1.5G 1 Sun solar irradiation.[47] Copyright 2021, Elsevier.

cell coupled to a triple-junction photovoltaic (TJ-PV) cell showed a CO_2 to CO STF efficiency of 23% (Fig. 16F).

Recently, a large-sized PV-EC system with a 1000 cm^2 irradiation area composed of five stacked electrodes (electrically parallel connected) and six series-connected single-crystalline Si PV cells was constructed by Kato and co-workers.[47] As illustrated in Fig. 16G and H, the anodes and cathodes ($\sim$1000 cm^2 in size) faced each other with a small distance of 1 cm in a transparent plastic housing without membrane separation and are directly connected to c-Si PV cells with similar sizes, which solves the proton diffusion resistance problem and avoids the use of a converter. The *I–V* curves of 6-series-connected single-crystalline Si PV cells and five stacked electrodes showed a good match between the EC reactor and PV cell (Fig. 16I), achieving a solar to formate conversion efficiency of 7.2%.

4. Conclusion and perspectives

At present, the highest achieved STF efficiencies for PC, PEC and PV-EC CO_2 reduction systems are $\sim$1%,[154] $\sim$10% (ref. 145) and $\sim$20%,[152,153] respectively. The PC, PEC systems are still confronted with the problems of low STF efficiency and poor stability. Only the PV-EC CO_2 reduction system showed an STF efficiency that meets industrial operation requirements. However, its high cost, poor stability and low selectivity for desired products limit its large-scale application. The photo-absorber, catalyst and device design, as three fundamental factors, collectively determine the solar-to-fuel efficiency of the system. It is essential to optimize the solar driven CO_2 reduction systems from a three-pronged approach and construct a system with these three elements optimized synergistically.

At present, the photo-absorbers suffer from low photo conversion efficiency and low stability. To improve the solar harvesting and conversion efficiency of the photo-absorbers, frequently used strategies are constructing heterojunction structures, elemental doping, nano-morphology control, defect engineering, amongst others. In addition, we can also explore new chemical functionalization, discover new semiconductors suitable for CO_2 reduction and construct composite photo-absorbers with multiple materials, such as organic semiconductors combined with inorganic semiconductors, biomimetic materials/biomaterials combined with inorganic semiconductors, or other newly developed photo-absorbers.

The catalysts, which promote CO_2 conversion, also require further development for reducing the reaction energy barriers and improving the product selectivity and stability. Although recent studies on the catalyst morphology control, bimetal or multi-metal construction, molecular catalyst modification, surface basic sites and the introduction of surface defects proved to be effective, there is still much work to be done. For example, we can construct a suitable reaction micro-environment that aims to achieve an appropriate local pH and surrounding ions for CO_2 reduction by chemical modification of the catalyst or specified nano-structure design of the catalysts using 3D printing or other techniques. To solve the problem of low CO_2 solubility in aqueous PC and PEC systems, materials with high CO_2 adsorption capacity can be applied to the catalysts. Furthermore, the synergetic operation of photo-absorbers and catalysts requires further in-depth exploration. With a clear mechanism of the interaction of photo-absorbers and catalysts during photochemical CO_2 reduction, a highly effective combination of photo-absorber and catalyst can be developed and the product selectivity can also be controlled by adjusting the combination strategy and mode.

The PC, PEC and PV-EC devices have been updated for several generations from the aspects of improving light absorption, enhancing the mass transfer and reducing the gas/liquid transfer resistance. As a result, the efficiency of CO_2 conversion has gradually increased. However, an optimized design for the devices remains challenging and demands suitable solutions to address key scientific and engineering problems. Accordingly, the following factors should be considered for the design of the device: the light source illumination way (built-in light, fiber lamp, *etc.*), mode of operation (batch, continuous flow, *etc.*), parameters of the chamber (volume, thickness, geometrical configuration, the in/out flow pathway of reactants, *etc.*) and membrane characteristics (for PEC and PV-EC systems). Meanwhile, we can also improve the reaction rate of product yields by designing a high pressure device for PC, PEC and PV-EC systems, since the solubility of CO_2 in aqueous media is a rate-limiting step in CO_2 reduction.

Finally, the synergetic operation of each component of the system is important for achieving high efficiency. The three key components, an efficient photo-absorber, a catalyst with high product selectivity and an optimized device design, working together synergistically will greatly improve the solar to fuel efficiency. The effect of how the photo-absorber and catalysts are combined, the light illumination method, device integration, and the supply of reactants on system efficiency requires further and systematic investigation.

Besides the scientific research of solar driven CO_2 reduction systems, great efforts should also be made on facilitating the industrial application of these technologies. The scale-up of existing high-performance systems is required in spite of the challenges faced with the optimization of the system parameters. For the scale-up of PC and PEC devices, it is necessary to design the devices in flow mode with multi-cells connected in series or parallels, and the problems of the increased resistance of aqueous solution and flowing gases need to be resolved. Furthermore, the efficient utilization of solar light must be considered when designing stacked devices. To improve the product yield rate of solar driven CO_2 reduction systems in practical use, high intensity light can be adopted. However, the low solubility of CO_2 in aqueous solution might hinder the reaction rate in this mode. We can refer to the flow cell design used for EC CO_2 reduction that separates the CO_2 gas from the aqueous solution and constructs a solid–liquid–gas triple-phase boundary for sufficient CO_2 supply. Due to the rapid development of PV cells and EC cells, there is a strong drive for PV-EC devices to reach maturity and be employed in industrial application. Nevertheless, it is essential to further improve the STF efficiency, optimize the selectivity, reduce the cost and improve the stability before industrial scale implementation. With the advantage of efficient thermal and flow field management, the integrated stacked PV-EC device will be a promising approach in the future. Inspired by the positive effect of external fields and inner micro-environments on the performance of EC devices,[91,155–159] the field or reaction environment effects should be thoroughly considered when designing the solar driven CO_2 reduction systems.

Conflicts of interest

There are no conflicts to declare.

Acknowledgements

J. L. acknowledges the funding support from the National Key Research and Development Program of China (2019YFE0123400 and 2022YFE0114800), the Excellent Young Scholar Fund from the National Natural Science Foundation of China (22122903), and the Tianjin Distinguished Young Scholar Fund (20JCJQJC00260). L. W. acknowledges the funding support from the Natural Science Foundation of China (grant no. 22209081) and the fellowship of China Postdoctoral Science Foundation (grant no. 2021M690082). J. L. and L. W. acknowledge the funding support from the Major Science and Technology Project of Anhui Province (202203f07020007).

References

1 H. Balat and C. Öz, *Energy Explor. Exploit.*, 2007, **25**, 357–392.
2 M. Mikkelsen, M. Jørgensen and F. C. Krebs, *Energy Environ. Sci.*, 2010, **3**, 43–81.
3 H. Yang, Z. Xu, M. Fan, R. Gupta, R. B. Slimane, A. E. Bland and I. Wright, *J. Environ. Sci.*, 2008, **20**, 14–27.
4 J. Ran, M. Jaroniec and S. Z. Qiao, *Adv. Mater.*, 2018, **30**, 1704649.
5 M. Halmann, *Nature*, 1978, **275**, 115–116.
6 W. J. Ong, L. K. Putri and A. R. Mohamed, *Chem.–Eur. J.*, 2020, **26**, 9710–9748.
7 X. Chang, T. Wang and J. Gong, *Energy Environ. Sci.*, 2016, **9**, 2177–2196.
8 J. L. White, M. F. Baruch, J. E. Pander III, Y. Hu, I. C. Fortmeyer, J. E. Park, T. Zhang, K. Liao, J. Gu and Y. Yan, *Chem. Rev.*, 2015, **115**, 12888–12935.
9 P. Usubharatana, D. McMartin, A. Veawab and P. Tontiwachwuthikul, *Ind. Eng. Chem. Res.*, 2006, **45**, 2558–2568.
10 S. Nitopi, E. Bertheussen, S. B. Scott, X. Liu, A. K. Engstfeld, S. Horch, B. Seger, I. E. Stephens, K. Chan and C. Hahn, *Chem. Rev.*, 2019, **119**, 7610–7672.
11 S. Xu and E. A. Carter, *Chem. Rev.*, 2018, **119**, 6631–6669.
12 M. Kibria, F. Chowdhury, S. Zhao, B. AlOtaibi, M. Trudeau, H. Guo and Z. Mi, *Nat. Commun.*, 2015, **6**, 1–8.
13 M. Schreier, F. Héroguel, L. Steier, S. Ahmad, J. S. Luterbacher, M. T. Mayer, J. Luo and M. Grätzel, *Nat. Energy*, 2017, **2**, 1–9.
14 M. T. Winkler, C. R. Cox, D. G. Nocera and T. Buonassisi, *Proc. Natl. Acad. Sci. U.S.A.*, 2013, **110**, 1076–1082.
15 C. E. Creissen and M. Fontecave, *Adv. Energy Mater.*, 2021, **11**, 2002652.
16 D. Li, K. Yang, J. Lian, J. Yan and S. Liu, *Adv. Energy Mater.*, 2022, **12**, 2201070.
17 T. N. Huan, D. A. Dalla Corte, S. Lamaison, D. Karapinar, L. Lutz, N. Menguy, M. Foldyna, S. H. Turren-Cruz, A. Hagfeldt and F. Bella, *Proc. Natl. Acad. Sci. U.S.A.*, 2019, **116**, 9735–9740.
18 J. L. White, J. T. Herb, J. J. Kaczur, P. W. Majsztrik and A. B. Bocarsly, *J. CO2 Util.*, 2014, **7**, 1–5.
19 X. Li, J. Yu, M. Jaroniec and X. Chen, *Chem. Rev.*, 2019, **119**, 3962–4179.
20 Q. Zhou, S. Ma and S. Zhan, *Appl. Catal. B Environ.*, 2018, **224**, 27–37.
21 V. Andrei, B. Reuillard and E. Reisner, *Nat. Mater.*, 2020, **19**, 189–194.
22 N. Zhang, R. Long, C. Gao and Y. Xiong, *Sci. China Mater.*, 2018, **61**, 771–805.
23 L. Liu, Y. Zhang and H. Huang, *Solar RRL*, 2021, **5**, 2000430.
24 O. Ola and M. M. Maroto-Valer, *J. Photochem. Photobiol., C*, 2015, **24**, 16–42.
25 V. P. Indrakanti, J. D. Kubicki and H. H. Schobert, *Energy Environ. Sci.*, 2009, **2**, 745–758.
26 Z. Xiong, Z. Lei, Y. Li, L. Dong, Y. Zhao and J. Zhang, *J. Photochem. Photobiol., C*, 2018, **36**, 24–47.
27 Y. Zhang, Z. Zhao, J. Chen, L. Cheng, J. Chang, W. Sheng, C. Hu and S. Cao, *Appl. Catal. B Environ.*, 2015, **165**, 715–722.
28 Y. Ma, X. Wang, Y. Jia, X. Chen, H. Han and C. Li, *Chem. Rev.*, 2014, **114**, 9987–10043.
29 A. Meng, B. Cheng, H. Tan, J. Fan, C. Su and J. Yu, *Appl. Catal. B Environ.*, 2021, **289**, 120039.
30 A. Ahmad Beigi, S. Fatemi and Z. Salehi, *J. CO_2 Util.*, 2014, **7**, 23–29.
31 A. Fujishima and K. Honda, *Nature*, 1972, **238**, 37–38.
32 T. Inoue, A. Fujishima, S. Konishi and K. Honda, *Nature*, 1979, **277**, 637–638.
33 Y. Xu, Y. Jia, Y. Zhang, R. Nie, Z. Zhu, J. Wang and H. Jing, *Appl. Catal. B Environ.*, 2017, **205**, 254–261.
34 S. K. Kuk, J. Jang, J. Kim, Y. Lee, Y. S. Kim, B. Koo, Y. W. Lee, J. W. Ko, B. Shin and J. K. Lee, *ChemSusChem*, 2020, **13**, 2940–2944.
35 J. Cheng, L. Wu and J. Luo, *Chem. Phys. Rev.*, 2022, **3**, 031306.
36 K. Tennakone, A. Jayatissa and S. Punchihewa, *J. Photochem. Photobiol., A*, 1989, **49**, 369–375.
37 M. E. Aguirre, R. Zhou, A. J. Eugene, M. I. Guzman and M. A. Grela, *Appl. Catal. B Environ.*, 2017, **217**, 485–493.
38 F. Zhang, Y. H. Li, M. Y. Qi, Z. R. Tang and Y. J. Xu, *Appl. Catal. B Environ.*, 2020, **268**, 118380.
39 M. Schreier, P. Gao, M. T. Mayer, J. Luo, T. Moehl, M. K. Nazeeruddin and S. D. T. andM. Grätzel, *Energy Environ. Sci.*, 2015, **8**, 855–861.
40 G. Liu, F. Zheng, J. Li, G. Zeng, Y. Ye, D. M. Larson, J. Yano, E. J. Crumlin, J. W. Ager, L. W. Wang and F. M. Toma, *Nat. Energy*, 2021, **6**, 1124–1132.

41 J. Gu, A. Wuttig, J. W. Krizan, Y. Hu, Z. M. Detweiler, R. J. Cava and A. B. Bocarsly, *J. Phys. Chem. C*, 2013, **117**, 12415–12422.
42 U. Kang, S. H. Yoon, D. S. Han and H. Park, *ACS Energy Lett.*, 2019, **4**, 2075–2080.
43 R. Hinogami, Y. Nakamura, S. Yae and Y. Nakato, *J. Phys. Chem. B*, 1998, **102**, 974–980.
44 S. K. Choi, U. Kang, S. Lee, D. J. Ham, S. M. Ji and H. Park, *Adv. Energy Mater.*, 2014, **4**, 1301614.
45 M. Kan, C. Yang, Q. Wang, Q. Zhang, Y. Yan, K. Liu, A. Guan and G. Zheng, *Adv. Energy Mater.*, 2022, **26**, 2201134.
46 I. Roh, S. Yu, C.-K. Lin, S. Louisia, S. Cestellos-Blanco and P. Yang, *J. Am. Chem. Soc.*, 2022, **144**, 8002–8006.
47 N. Kato, S. Mizuno, M. Shiozawa, N. Nojiri, Y. Kawai, K. Fukumoto, T. Morikawa and Y. Takeda, *Joule*, 2021, **5**, 687–705.
48 J. Kim, S. Jeong, M. Beak, J. Park and K. Kwon, *Chem. Eng. J.*, 2022, **428**, 130259.
49 E. E. Barton, D. M. Rampulla and A. B. Bocarsly, *J. Am. Chem. Soc.*, 2008, **130**, 6342–6344.
50 G. Zeng, J. Qiu, Z. Li, P. Pavaskar and S. B. Cronin, *ACS Catal.*, 2014, **4**, 3512–3516.
51 M. Lessio and E. A. Carter, *J. Am. Chem. Soc.*, 2015, **137**, 13248–13251.
52 L. Cheng, Q. Xiang, Y. Liao and H. Zhang, *Energy Environ. Sci.*, 2018, **11**, 1362–1391.
53 K. Yang, Z. Yang, C. Zhang, Y. Gu, J. Wei, Z. Li, C. Ma, X. Yang, K. Song and Y. Li, *Chem. Eng. J.*, 2021, **418**, 129344.
54 J. Low, B. Dai, T. Tong, C. Jiang and J. Yu, *Adv. Mater.*, 2019, **31**, 1802981.
55 Z. Zhu, J. Qin, M. Jiang, Z. Ding and Y. Hou, *Appl. Surf. Sci.*, 2017, **391**, 572–579.
56 J. Luo, M. T. Mayer and M. Grätzel, in *Organic-Inorganic Halide Perovskite Photovoltaics: From Fundamentals to Device Architectures*, ed. N.-G. Park, M. Grätzel and T. Miyasaka, Springer International Publishing, Cham, 2016, pp. 285–305.
57 M. Schreier, L. Curvat, F. Giordano, L. Steier, A. Abate, S. M. Zakeeruddin, J. Luo, M. T. Mayer and M. Grätzel, *Nat. Commun.*, 2015, **6**, 1–6.
58 L. Y. Wu, Y. F. Mu, X. X. Guo, W. Zhang, Z. M. Zhang, M. Zhang and T. B. Lu, *Angew. Chem., Int. Ed.*, 2019, **58**, 9491–9495.
59 R. Chen, G. Gao and J. Luo, *Nano Res.*, 2022, **15**, 10084–10089.
60 Y. F. Xu, M. Z. Yang, B. X. Chen, X. D. Wang, H. Y. Chen, D. B. Kuang and C. Y. Su, *J. Am. Chem. Soc.*, 2017, **139**, 5660–5663.
61 Y. X. Chen, Y. F. Xu, X. D. Wang, H. Y. Chen and D. B. Kuang, *Sustain. Energy Fuels*, 2020, **4**, 2249–2255.
62 K. Su, G. X. Dong, W. Zhang, Z. L. Liu, M. Zhang and T. B. Lu, *ACS Appl. Mater. Interfaces*, 2020, **12**, 50464–50471.
63 H. Li, J. Li, Z. Ai, F. Jia and L. Zhang, *Angew. Chem., Int. Ed.*, 2018, **57**, 122–138.
64 T. D. Nguyen, C. T. Dinh and T. O. Do, *Chem. Commun.*, 2015, **51**, 624–635.
65 M. Irfan, M. Sevim, Y. Koçak, M. Balci, Ö. Metin and E. Ozensoy, *Appl. Catal. B Environ.*, 2019, **249**, 126–137.
66 G. Dong and L. Zhang, *J. Mater. Chem.*, 2012, **22**, 1160–1166.
67 J. Mao, T. Peng, X. Zhang, K. Li, L. Ye and L. Zan, *Catal. Sci. Technol.*, 2013, **3**, 1253–1260.
68 K. Wang, Q. Li, B. Liu, B. Cheng, W. Ho and J. Yu, *Appl. Catal. B Environ.*, 2015, **176–177**, 44–52.
69 M. Volokh, G. Peng, J. Barrio and M. Shalom, *Angew. Chem., Int. Ed.*, 2019, **58**, 6138–6151.
70 N. Sagara, S. Kamimura, T. Tsubota and T. Ohno, *Appl. Catal. B Environ.*, 2016, **192**, 193–198.
71 Q. Wang, X. Wang, Z. Yu, X. Jiang, J. Chen, L. Tao, M. Wang and Y. Shen, *Nano Energy*, 2019, **60**, 827–835.
72 A. E. Baumann, D. A. Burns, B. Liu and V. S. Thoi, *Commun. Chem.*, 2019, **2**, 86.
73 A. E. Baumann, D. A. Burns, B. Liu and V. S. Thoi, *Commun. Chem.*, 2019, **2**, 1–14.
74 Q. Wang, Y. Zhang, H. Lin and J. Zhu, *Chem.–Eur. J.*, 2019, **25**, 14026–14035.
75 T. Zhang and W. Lin, *Chem. Soc. Rev.*, 2014, **43**, 5982–5993.
76 A. Dhakshinamoorthy, A. M. Asiri and H. Garcia, *Angew. Chem., Int. Ed.*, 2016, **55**, 5414–5445.
77 S. Wang and X. Wang, *Small*, 2015, **11**, 3097–3112.
78 C. Wang, Z. Xie, K. E. deKrafft and W. Lin, *J. Am. Chem. Soc.*, 2011, **133**, 13445–13454.
79 Y. Fu, D. Sun, Y. Chen, R. Huang, Z. Ding, X. Fu and Z. Li, *Angew. Chem., Int. Ed.*, 2012, **51**, 3364–3367.
80 H. Q. Xu, J. Hu, D. Wang, Z. Li, Q. Zhang, Y. Luo, S. H. Yu and H. L. Jiang, *J. Am. Chem. Soc.*, 2015, **137**, 13440–13443.
81 Y. C. Hao, L. W. Chen, J. Li, Y. Guo, X. Su, M. Shu, Q. Zhang, W. Y. Gao, S. Li and Z. L. Yu, *Nat. Commun.*, 2021, **12**, 1–11.
82 I. I. Alkhatib, C. Garlisi, M. Pagliaro, K. Al-Ali and G. Palmisano, *Catal. Today*, 2020, **340**, 209–224.
83 X. Li and Q. L. Zhu, *EnergyChem*, 2020, **2**, 100033.
84 Z. Qin, J. Wu, B. Li, T. Su and H. Ji, *Acta Phys.-Chim. Sin.*, 2021, **37**, 2005027.
85 Z. Sun, N. Talreja, H. Tao, J. Texter, M. Muhler, J. Strunk and J. Chen, *Angew. Chem., Int. Ed.*, 2018, **57**, 7610–7627.
86 X. Chang, T. Wang, P. Yang, G. Zhang and J. Gong, *Adv. Mater.*, 2019, **31**, 1804710.
87 C. Yang, S. Li, Z. Zhang, H. Wang, H. Liu, F. Jiao, Z. Guo, X. Zhang and W. Hu, *Small*, 2020, **16**, 2001847.
88 Q. Yang, Q. Wu, Y. Liu, S. Luo, X. Wu, X. Zhao, H. Zou, B. Long, W. Chen and Y. Liao, *Adv. Mater.*, 2020, **32**, 2002822.
89 L. Wan, X. Zhang, J. Cheng, R. Chen, L. Wu, J. Shi and J. Luo, *ACS Catal.*, 2022, **12**, 2741–2748.
90 Q. Chen, K. Liu, Y. Zhou, X. Wang, K. Wu, H. Li, E. Pensa, J. Fu, M. Miyauchi, E. Cortés and M. Liu, *Nano Lett.*, 2022, **22**, 6276–6284.
91 C. Cai, B. Liu, K. Liu, P. Li, J. Fu, Y. Wang, W. Li, C. Tian, Y. Kang and A. Stefancu, *Angew. Chem., Int. Ed.*, 2022, **61**, e202212640.
92 Q. Wang, K. Liu, K. Hu, C. Cai, H. Li, H. Li, M. Herran, Y.-R. Lu, T.-S. Chan, C. Ma, J. Fu, S. Zhang, Y. Liang, E. Cortés and M. Liu, *Nat. Commun.*, 2022, **13**, 6082.

93 L. Han, S. Song, M. Liu, S. Yao, Z. Liang, H. Cheng, Z. Ren, W. Liu, R. Lin, G. Qi, X. Liu, Q. Wu, J. Luo and H. L. Xin, *J. Am. Chem. Soc.*, 2020, **142**, 12563–12567.
94 C. Choi, S. Kwon, T. Cheng, M. Xu, P. Tieu, C. Lee, J. Cai, H. M. Lee, X. Pan, X. Duan, W. A. Goddard and Y. Huang, *Nat. Catal.*, 2020, **3**, 804–812.
95 Y. Zhou, A. J. Martín, F. Dattila, S. Xi, N. López, J. Pérez-Ramírez and B. S. Yeo, *Nat. Catal.*, 2022, **5**, 545–554.
96 J. T. Song, H. Ryoo, M. Cho, J. Kim, J. G. Kim, S. Y. Chung and J. Oh, *Adv. Energy Mater.*, 2017, **7**, 1601103.
97 M. Tahir, B. Tahir and N. A. S. Amin, *Appl. Catal. B Environ.*, 2017, **204**, 548–560.
98 J. Qu, X. Zhang, Y. Wang and C. Xie, *Electrochim. Acta*, 2005, **50**, 3576–3580.
99 Q. Xiang, J. Yu and M. Jaroniec, *J. Am. Chem. Soc.*, 2012, **134**, 6575–6578.
100 J. Low, L. Zhang, T. Tong, B. Shen and J. Yu, *J. Catal.*, 2018, **361**, 255–266.
101 K. K. Sakimoto, A. B. Wong and P. Yang, *Science*, 2016, **351**, 74–77.
102 Y. Hori, A. Murata and R. Takahashi, *J. Chem. Soc. Faraday Trans. I*, 1989, **85**, 2309–2326.
103 W. Liu, P. Zhai, A. Li, B. Wei, K. Si, Y. Wei, X. Wang, G. Zhu, Q. Chen, X. Gu, R. Zhang, W. Zhou and Y. Gong, *Nat. Commun.*, 2022, **13**, 1877.
104 Y. Zhou, Y. Liang, J. Fu, K. Liu, Q. Chen, X. Wang, H. Li, L. Zhu, J. Hu, H. Pan, M. Miyauchi, L. Jiang, E. Cortés and M. Liu, *Nano Lett.*, 2022, **22**, 1963–1970.
105 Y. Hu, F. Chen, P. Ding, H. Yang, J. Chen, C. Zha and Y. Li, *J. Mater. Chem. A*, 2018, **6**, 21906–21912.
106 J. Qiu, G. Zeng, M.-A. Ha, M. Ge, Y. Lin, M. Hettick, B. Hou, A. N. Alexandrova, A. Javey and S. B. Cronin, *Nano Lett.*, 2015, **15**, 6177–6181.
107 J. S. DuChene, G. Tagliabue, A. J. Welch, W.-H. Cheng and H. A. Atwater, *Nano Lett.*, 2018, **18**, 2545–2550.
108 S. Xie, Y. Wang, Q. Zhang, W. Deng and Y. Wang, *ACS Catal.*, 2014, **4**, 3644–3653.
109 W. N. Wang, W. J. An, B. Ramalingam, S. Mukherjee, D. M. Niedzwiedzki, S. Gangopadhyay and P. Biswas, *J. Am. Chem. Soc.*, 2012, **134**, 11276–11281.
110 G. Gao, Y. Jiao, E. R. Waclawik and A. Du, *J. Am. Chem. Soc.*, 2016, **138**, 6292–6297.
111 K. Iizuka, T. Wato, Y. Miseki, K. Saito and A. Kudo, *J. Am. Chem. Soc.*, 2011, **133**, 20863–20868.
112 Z. Wang, K. Teramura, S. Hosokawa and T. Tanaka, *J. Mater. Chem. A*, 2015, **3**, 11313–11319.
113 W. Kim, T. Seok and W. Choi, *Energy Environ. Sci.*, 2012, **5**, 6066–6070.
114 S. Bai, X. Wang, C. Hu, M. Xie, J. Jiang and Y. Xiong, *Chem. Commun.*, 2014, **50**, 6094–6097.
115 N. Sasirekha, S. J. S. Basha and K. Shanthi, *Appl. Catal. B Environ.*, 2006, **62**, 169–180.
116 L. Cao, S. Sahu, P. Anilkumar, C. E. Bunker, J. Xu, K. S. Fernando, P. Wang, E. A. Guliants, K. N. Tackett and Y.-P. Sun, *J. Am. Chem. Soc.*, 2011, **133**, 4754–4757.
117 Q. Kong, D. Kim, C. Liu, Y. Yu, Y. Su, Y. Li and P. Yang, *Nano Lett.*, 2016, **16**, 5675–5680.
118 X. Zhang, F. Han, B. Shi, S. Farsinezhad, G. P. Dechaine and K. Shankar, *Angew. Chem., Int. Ed.*, 2012, **51**, 12732–12735.
119 X. Yang, E. A. Fugate, Y. Mueanngern and L. R. Baker, *ACS Catal.*, 2017, **7**, 177–180.
120 P. Shao, S. Ci, L. Yi, P. Cai, P. Huang, C. Cao and Z. Wen, *ChemElectroChem*, 2017, **4**, 2593–2598.
121 W. J. Dong, I. A. Navid, Y. Xiao, J. W. Lim, J. L. Lee and Z. Mi, *J. Am. Chem. Soc.*, 2021, **143**, 10099–10107.
122 S. C. Yan, S. X. Ouyang, J. Gao, M. Yang, J. Y. Feng, X. X. Fan, L. J. Wan, Z. S. Li, J. H. Ye and Y. Zhou, *Angew. Chem.*, 2010, **122**, 6544–6548.
123 W. Tu, Y. Li, L. Kuai, Y. Zhou, Q. Xu, H. Li, X. Wang, M. Xiao and Z. Zou, *Nanoscale*, 2017, **9**, 9065–9070.
124 T. W. Woolerton, S. Sheard, E. Reisner, E. Pierce, S. W. Ragsdale and F. A. Armstrong, *J. Am. Chem. Soc.*, 2010, **132**, 2132–2133.
125 H. Shen, T. Peppel, J. Strunk and Z. Sun, *Solar RRL*, 2020, **4**, 1900546.
126 Y. Su, S. Cestellos-Blanco, J. M. Kim, Y.-x. Shen, Q. Kong, D. Lu, C. Liu, H. Zhang, Y. Cao and P. Yang, *Joule*, 2020, **4**, 800–811.
127 Q. Wang, S. Kalathil, C. Pornrungroj, C. D. Sahm and E. Reisner, *Nat. Catal.*, 2022, **5**, 633–641.
128 P. Yue, in *Photoelectrochemistry, Photocatalysis and Photoreactors*, Springer, 1985, pp. 527–547.
129 A. A. Khan and M. Tahir, *J. CO_2 Util.*, 2019, **29**, 205–239.
130 L. Wan, Q. Zhou, X. Wang, T. E. Wood, L. Wang, P. N. Duchesne, J. Guo, X. Yan, M. Xia, Y. F. Li, A. A. Jelle, U. Ulmer, J. Jia, T. Li, W. Sun and G. A. Ozin, *Nat. Catal.*, 2019, **2**, 889–898.
131 S. Bai, H. Qiu, M. Song, G. He, F. Wang, Y. Liu and L. Guo, *eScience*, 2022, **2**, 428–437.
132 I. H. Tseng, W. C. Chang and J. C. Wu, *Appl. Catal. B Environ.*, 2002, **37**, 37–48.
133 P. Zhang, S. Wang, B. Y. Guan and X. W. D. Lou, *Energy Environ. Sci.*, 2019, **12**, 164–168.
134 M. Tahir and N. S. Amin, *Appl. Catal. B Environ.*, 2013, **142**, 512–522.
135 E. G. Look and H. D. Gafney, *J. Phys. Chem. A*, 2013, **117**, 12268–12279.
136 M. Tahir and N. S. Amin, *Appl. Catal., A*, 2013, **467**, 483–496.
137 S. Ali, J. Lee, H. Kim, Y. Hwang, A. Razzaq, J. W. Jung, C. H. Cho and S. I. In, *Appl. Catal. B Environ.*, 2020, **279**, 119344.
138 H. Huang, R. Shi, Z. Li, J. Zhao, C. Su and T. Zhang, *Angew. Chem.*, 2022, **134**, e202200802.
139 H. Homayoni, W. Chanmanee, N. R. de Tacconi, B. H. Dennis and K. Rajeshwar, *J. Electrochem. Soc.*, 2015, **162**, E115.
140 E. Kalamaras, M. Belekoukia, J. Z. Tan, J. Xuan, M. M. Maroto-Valer and J. M. Andresen, *Faraday Discuss*, 2019, **215**, 329–344.
141 V. Kumaravel, J. Bartlett and S. C. Pillai, *ACS Energy Lett.*, 2020, **5**, 486–519.
142 V. Andrei, G. M. Ucoski, C. Pornrungroj, C. Uswachoke, Q. Wang, D. S. Achilleos, H. Kasap, K. P. Sokol, R. A. Jagt, H. Lu, T. Lawson, A. Wagner, S. D. Pike, D. S. Wright,

R. L. Z. Hoye, J. L. MacManus-Driscoll, H. J. Joyce, R. H. Friend and E. Reisner, *Nature*, 2022, **608**, 518–522.

143 S. Castro, J. Albo and A. Irabien, *ACS Sustainable Chem. Eng.*, 2018, **6**, 15877–15894.

144 Y. C. Li, D. Zhou, Z. Yan, R. H. Gonçalves, D. A. Salvatore, C. P. Berlinguette and T. E. Mallouk, *ACS Energy Lett.*, 2016, **1**, 1149–1153.

145 X. Zhou, R. Liu, K. Sun, Y. Chen, E. Verlage, S. A. Francis, N. S. Lewis and C. Xiang, *ACS Energy Lett.*, 2016, **1**, 764–770.

146 S. Sultan, J. H. Kim, S. Kim, Y. Kwon and J. S. Lee, *J. Energy Chem.*, 2021, **60**, 410–416.

147 A. J. Bard and M. A. Fox, *Acc. Chem. Res.*, 1995, **28**, 141–145.

148 T. Sekimoto, S. Shinagawa, Y. Uetake, K. Noda, M. Deguchi, S. Yotsuhashi and K. Ohkawa, *Appl. Phys. Lett.*, 2015, **106**, 073902.

149 D. Ren, N. W. X. Loo, L. Gong and B. S. Yeo, *ACS Sustain. Chem. Eng.*, 2017, **5**, 9191–9199.

150 T. Arai, S. Sato and T. Morikawa, *Energy Environ. Sci.*, 2015, **8**, 1998–2002.

151 J. Bullock, D. F. Srankó, C. M. Towle, Y. Lum, M. Hettick, M. Scott, A. Javey and J. Ager, *Energy Environ. Sci.*, 2017, **10**, 2222–2230.

152 J. Gao, J. Li, Y. Liu, M. Xia, Y. Z. Finfrock, S. M. Zakeeruddin, D. Ren and M. Grätzel, *Nat. Commun.*, 2022, **13**, 5898.

153 M. Asadi, M. H. Motevaselian, A. Moradzadeh, L. Majidi, M. Esmaeilirad, T. V. Sun, C. Liu, R. Bose, P. Abbasi and P. Zapol, *Adv. Energy Mater.*, 2019, **9**, 1803536.

154 S. Sorcar, J. Thompson, Y. Hwang, Y. H. Park, T. Majima, C. A. Grimes, J. R. Durrant and S. I. In, *Energy Environ. Sci.*, 2018, **11**, 3183–3193.

155 M. Liu, Y. Pang, B. Zhang, P. De Luna, O. Voznyy, J. Xu, X. Zheng, C. T. Dinh, F. Fan, C. Cao, F. P. G. de Arquer, T. S. Safaei, A. Mepham, A. Klinkova, E. Kumacheva, T. Filleter, D. Sinton, S. O. Kelley and E. H. Sargent, *Nature*, 2016, **537**, 382–386.

156 B. Yang, K. Liu, H. Li, C. Liu, J. Fu, H. Li, J. E. Huang, P. Ou, T. Alkayyali, C. Cai, Y. Duan, H. Liu, P. An, N. Zhang, W. Li, X. Qiu, C. Jia, J. Hu, L. Chai, Z. Lin, Y. Gao, M. Miyauchi, E. Cortés, S. A. Maier and M. Liu, *J. Am. Chem. Soc.*, 2022, **144**, 3039–3049.

157 A. Ozden, F. P. García de Arquer, J. E. Huang, J. Wicks, J. Sisler, R. K. Miao, C. P. O'Brien, G. Lee, X. Wang, A. H. Ip, E. H. Sargent and D. Sinton, *Nat. Sustain.*, 2022, **5**, 563–573.

158 M. Zhong, K. Tran, Y. Min, C. Wang, Z. Wang, C.-T. Dinh, P. De Luna, Z. Yu, A. S. Rasouli and P. Brodersen, *Nature*, 2020, **581**, 178–183.

159 K. Xie, R. K. Miao, A. Ozden, S. Liu, Z. Chen, C.-T. Dinh, J. E. Huang, Q. Xu, C. M. Gabardo, G. Lee, J. P. Edwards, C. P. O'Brien, S. W. Boettcher, D. Sinton and E. H. Sargent, *Nat. Commun.*, 2022, **13**, 3609.